Title:

Spectral signatures of feedforward and recurrent circuitry in monkey area MT

Running Title:

Signatures of feedforward and recurrent circuitry

Authors:

Selina S. Solomon [1,2,], John W. Morley[3], Samuel G. Solomon[4]

Author Affiliations:

1. Discipline of Physiology, School of Medical Sciences and Bosch Institute, The University of Sydney, NSW 2006, Australia.
2. Dominick P. Purpura Department of Neuroscience, Albert Einstein College of Medicine, Rose F. Kennedy Center Room 822, 1410 Pelham Parkway South, Bronx NY 10461, USA.
3. School of Medicine, University of Western Sydney, Campbelltown, NSW 2560, Australia
4. Department of Experimental Psychology, University College London, WC1P 0AH, UK

Corresponding Author:

Selina S. Solomon (selina.solomon@einstein.yu.edu)

Albert Einstein College of Medicine, Rose F. Kennedy Center Room 822, 1410 Pelham Parkway South, Bronx NY 10461, USA.

Phone: +1(718) 430-2418.

ABSTRACT

Recordings of local field potential (LFP) in the visual cortex can show rhythmic activity at gamma frequencies (30-100 Hz). While the gamma rhythms in primary visual cortex have been well studied, the structural and functional characteristics of gamma rhythms in extrastriate visual cortex are less clear. Here we studied the spatial distribution and functional specificity of gamma rhythms in extrastriate middle temporal (MT) area of visual cortex in marmoset monkeys. We found that moving gratings induced narrowband gamma rhythms across cortical layers, that were coherent across much of area MT. Moving dot fields instead induced broadband increase in LFP in middle and upper layers, with weaker narrowband gamma rhythms in deeper layers. The stimulus-dependence of LFP response in middle- and upper layers of area MT appears to reflect the presence (gratings) or absence (dot fields and other textures) of strongly oriented contours. Our results suggest that gamma rhythms in these layers are propagated from earlier visual cortex, while those in the deeper layers may emerge in area MT.

Keywords: area MT; gamma; LFP; motion processing; visual pathways

INTRODUCTION

Rhythmic electrical activity at temporal frequencies in the gamma-band (30-100 Hz) is prominent in several brain areas. In mesoscopic measurements such as the local field potential (LFP), these gamma rhythms may manifest as a narrow 'bump' in the power spectrum (Fries et al., 2001). In the primate visual system, gamma rhythms in primary visual cortex (area V1) have now been well characterized (Henrie and Shapley, 2005, Bartolo et al., 2011, Lima et al., 2010, Ray and Maunsell, 2011a, Jia et al., 2013a, Jia et al., 2013b, Maier et al., 2010, Chalk et al., 2010, Berens et al., 2008, Gail et al., 2000, Bastos et al., 2014). The gamma rhythms in V1 LFP are entrained with spiking activity (Gieselmann and Thiele, 2008, Jia et al., 2013a), particularly in superficial layers of V1 that are the major source of output to other cortical areas (Buffalo et al., 2011).

The gamma rhythm in V1 is likely to arise from the activity of intrinsic neural networks involving GABAergic interneurons (Buzsaki and Wang, 2012, Whittington et al., 2011). Similar circuits in extrastriate areas are presumably capable of generating gamma rhythms, but evidence for gamma rhythms in extrastriate visual areas is capricious: they have been observed in some previous work (Fries et al., 2001, Fries et al., 2008, Ray et al., 2013), but not in others (Esghaei and Daliri, 2014, Khayat et al., 2010, Liu and Newsome, 2006). Even when found, it is unclear if these rhythms emerge in networks that are intrinsic to extrastriate areas, or reflect rhythms propagated from earlier visual cortex (van Kerkoerle et al., 2014, Bastos et al., 2015). Knowledge of the spatial structure and functional specificity of gamma rhythms in extrastriate cortex would help clarify where they emerge, but previous work has not provided this information.

We measured gamma rhythms in the LFP signal recorded from extrastriate

area MT, a well-studied area of the primate cortex that is important for motion vision. We took advantage of the smooth topology of the marmoset monkey brain, where most visual areas, including area MT, lie exposed on the cortical surface. This allowed us to measure the distribution of gamma rhythms across the two axes of the cortical sheet. To distinguish propagated rhythms from intrinsic rhythms, we compared visually induced LFP response in presence (moving gratings) and absence (moving dot fields) of oriented contours. Both stimuli elicit strong responses from neurons in area MT. Gratings are known to induce prominent gamma rhythms in area V1, which we confirm here. By contrast, strong gamma rhythms are not observed in V1 for broadband or noisy stimuli (Jia et al., 2011, Hermes et al., 2015), and we show that they are also absent during presentation of dot fields. In area MT, we found that gamma rhythms in the middle and upper layers require oriented contours, and may largely reflect gamma rhythms propagated from area V1. Gamma rhythms in the deep layers, however, can also be induced by dot fields, and may emerge within area MT.

MATERIALS AND METHODS

Ethical Approval

Nine adult marmosets (*Callithrix jacchus*; 7 males; weight 290–400 g) were obtained from the Australian National Health and Medical Research Council (NHMRC) combined breeding facility. Procedures were approved by Institutional (University of Sydney) Animal Ethics Committee and conform to the Society for Neuroscience and NHMRC policies on the use of animals in neuroscience research.

Experimental Preparation

The measurements here were obtained during a larger series of experiments reported elsewhere (Solomon et al., 2015, McDonald et al., 2014). Full details of experimental preparation can be found in those reports. Briefly, during measurements anesthesia and analgesia were maintained by intravenous infusion of sufentanil (6–30 $\mu g\ kg^{-1}\ h^{-1}$) in physiological solution, and inspired 70:30 mix of N_2O and carbogen. Dominance of low frequencies (1–5 Hz) in the electroencephalogram (EEG) recording, and absence of EEG changes under noxious stimulus (tail pinch) were used as the chief sign of an adequate level of anesthesia. At any sign of the anaesthesia becoming less effective the dose of sufentanil citrate was increased. Muscular paralysis was maintained by infusion of pancuronium bromide (0.3 mg/kg/hr). The corneas were protected with high-permeability contact lenses; no artificial pupils were used. At the end of the experiment, the animal was euthanized with intravenous 500 mg/kg sodium pentobarbitone (Lethobarb; Verbac Australia). The animal was perfused transcardially with 0.9% sodium chloride and then 4% paraformaldehyde in

0.1 M phosphate buffer, following which the brain was removed and post-fixed for 24 h. The tissue was then transferred to a 30% sucrose solution in 0.1 M phosphate buffer.

In 5 animals extracellular recordings were obtained from area MT using a 10 × 10 grid of parylene-coated platinum iridium microelectrodes (1.5 mm in length, spacing 0.4 mm; Blackrock Microsystems), inserted to a depth of approximately 1 mm. From the trajectory of receptive field positions (Rosa and Elston, 1998), we identified electrodes likely to be within area MT, and others likely to be in area MTc (a thin area that borders much of anterior MT). Of the 96 recording electrodes, average 63.0% (range 40.6–87.5%) were classified as within area MT and 18.9% (range 10.4–33.3%) were classified as within area MTc. We include measurements from electrodes in both regions; excluding measurements from area MTc did not qualitatively change any results. In 3 other animals, we made 12 insertions into area MT of an array (NeuroNexus) of 8 laminar probes (spacing 0.2 mm), each of which had 8 iridium contact points (spacing 0.2 mm). In 1 additional animal, we used these laminar probes to make 3 penetrations into V1 across 2 hemispheres.

Visual stimuli and recording

Visual stimuli were drawn by custom software (EXPO; P. Lennie) running on a G5 Power Macintosh computer and displayed on a calibrated cathode ray tube monitor (Sony G520, refresh rate 100 Hz, mean luminance 45–55 cd/m^2, width 40 cm and height 30 cm), viewed at a distance of 114 cm via a front-silvered mirror (V1 recordings), or directly at 45 cm (MT recordings). Supplementary lenses were used to focus the eyes. During measurements, one eye, usually the contralateral eye, was occluded.

Signals from each electrode were amplified, filtered and digitised by an RZ2 real-time processor (Tucker-Davis Technologies). For LFP, signals were bandpass-filtered (0.7 – 300 Hz) and digitized at a rate of 1.02 kHz. For spiking activity, signals were bandpass-filtered (0.3 – 5 kHz) and digitized at a rate of 24 kHz. All offline analyses were conducted in the Matlab environment (MathWorks Inc., Natick, MA). The function *findpeaks* was used to identify candidate (multi-unit) waveforms with peak amplitudes that exceeded 3 standard deviations of the raw 'spike signal' on the relevant channel. Details of single-unit spike sorting can be found in Solomon et al. (2015). No response criterion was imposed for measurements of spike-field coherence and auto-correlograms. Multi-unit spike trains (bin width 0.1 ms) and single-unit spike trains (bin width 1 ms) were used to compute auto-correlograms (Perkel et al., 1967, Bair et al., 2001)

Datasets

Most of our quantitative analyses use measurements obtained during long (2 s) presentations of dot fields or gratings, described in Solomon et al. (2015). These were obtained in separate recording epochs, separated by 5-240 minutes. To characterise stimulus sensitivity of LFP, we made additional measurements during brief presentations of parametrically varying stimuli.

Long presentations

Dot fields comprised white circular dots (diameter 0.4 degrees; Weber contrast 1.0) that translated across the monitor screen; outside each dot the monitor was held at the mean luminance. Gratings were drifting sine-wave gratings (Michelson contrast

0.5, spatial frequency 0.2-0.5 cycles/degree; temporal frequency 4-5 Hz except in one animals where the temporal frequency was 8 Hz). These spatial frequencies were chosen to drive most neurons in marmoset area MT, across the range of retinal eccentricities (Lui et al., 2007). For both dot fields and gratings, different motion directions (90 degree steps) were presented in pseudorandom order for 2 s within a large circular window (MT: diameter 30 degrees; V1: 14 degrees); between each stimulus the screen was held at the mean luminance for 2 s. We obtained responses to 100 trials of each stimulus. Single-unit spiking activity during presentation of these stimuli has been reported previously (Solomon et al., 2015).

Brief presentations

Each set of stimuli, which included a grey screen in addition to the visual patterns, were presented in a pseudorandom order.

Set (1): includes drifting gratings at each of 12 directions (30 degree steps), 3 spatial frequencies (0.1, 0.3,1.0 cycles/deg), and 3 temporal frequencies (2.5, 7.7, 25 Hz). Each trial lasted for 0.5 s and between each trial the screen was held at the mean luminance for 0.05 s. Measurements were made for 20 trials of each stimulus.

Set (2): includes dot fields or gratings at each of 8 directions (45 degree steps) at each of three contrasts (dot fields: Weber contrast 0.25, 0.5, 1.0; gratings: Michelson contrast 0.125, 0.35, 1.0). For gratings, temporal frequency was 5 Hz, spatial frequency was 0.2 cycles/degree (2 recordings) or 0.8 cycles/degree (1 recording). Each trial lasted for 0.3 s and between each trial the screen was held at the mean luminance for 0.3 s. Measurements were made for 100 trials of each stimulus.

Set (3): includes static gratings (0.4 cycles/degree, Michelson contrast 0.125) and moving synthetic textures, at each of 12 motion directions (30 degree steps).

Construction of the textures has been described elsewhere (Goddard et al., 2008, Gharaei et al., 2013). Briefly, textures were random noise filtered by a log-Gaussian over spatial frequency (centre frequency ~0.2 cycles/degree; bandwidth 0.5 octaves) and a Gaussian over orientation (SD 6.3 or 25 degrees). Each texture was 256 x 256 pixels and the centre pixel was indexed [129,129]. To generate the filters, two coordinate matrices of the same size were created; one matrix specified the distribution of Fourier amplitude over spatial frequency (distance of each pixel from the centre pixel) and the other matrix specified the distribution of Fourier amplitude over orientation (angle of each pixel relative to the centre pixel). These two matrices were multiplied together to provide a distribution of Fourier amplitude over spatial frequency and orientation. The resultant was then shifted using the function *fftshift* in Matlab and used to filter uniformly distributed random noise to generate the synthetic textures. Images were normalized so that the root-mean-square pixel contrast was in each case 0.125. The consequence of this normalisation is that as more orientations are included in each texture, the Fourier amplitude along the dominant orientation axis declines. Stimuli were viewed through a large circular aperture (diameter 35 or 45 degrees). Each trial lasted 0.3 s, between which the screen was held at the mean luminance for 0.3 s. Measurements were made for 25 trials of each stimulus.

LFP signal processing

Removal of line noise

To remove line noise (50 Hz) and its harmonics, we first applied a second-order Butterworth band-stop filter (bandwidth 0.5 Hz) to the raw LFP signals recorded from all electrodes. LFP was further filtered using second or third order

Butterworth filters, tailored for each electrode, until there were no sharp peaks at 50 Hz and its harmonics. Zero-phase forward and reverse filtering was performed using the function *filtfilt* in Matlab.

LFP signal analysis.

The LFP response on a single trial is composed of two components: the stimulus-evoked component and the stimulus-induced component. The stimulus-evoked component is referenced to the time of stimulus onset and has been included in previous work in area MT (Khawaja et al., 2009, Liu and Newsome, 2006, Khayat et al., 2010, Esghaei and Daliri, 2014, Ray et al., 2013). Here we focus our analyses on the induced component that captures activity that is not time-locked to stimulus onset. The evoked LFP was defined as the mean LFP signal across trials:

$$LFP_{evoked}(s,t) = \frac{1}{N}\sum_{i}^{N} LFP_i(s,t) \qquad \text{Equation 1}$$

where s is the stimulus condition, t is time, N is the number of trials and LFP_i is the signal on the i-th trial. The stimulus-induced LFP was estimated by subtracting the stimulus-evoked LFP from the LFP measured on each trial:

$$LFP_{induced}(s,i) = LFP_i(s,t) - LFP_{evoked}(s,t) \qquad \text{Equation 2}$$

Similar measurements were made during the presentation of grey screens. For consistency, we subtracted the mean LFP from the trial-by-trial measures of maintained activity ('evoked LFP' for a grey screen); including the mean component did not qualitatively change the results.

Multi-taper analysis

Time-frequency multi-taper spectral analysis was performed (Thomson, 1982) on the induced LFP using Chronux (http://www.chronux.org/ (Bokil et al., 2010), for

frequencies between 0.7 and 250 Hz. The parameters for the multi-taper analysis (Table 1) were adjusted for each stimulus set to provide reasonable smoothing in frequency space without introducing excessive distortion in the power spectra. For consistency, we used the same parameters across electrodes and across animals. This resulted in some measurements showing distortions that appear as 'ripples' in the coherence-frequency plots. The power at each time-frequency point was computed using the function *mtspecgramc*. The coherence at each time-frequency point was computed using the function *cohgramc* (for LFP-LFP coherence) or *cohgramcpt* (for spike-LFP coherence). The stimulus-induced power is the ratio of the power at each time-frequency point during visual stimulation to the mean power measured for that frequency during maintained activity (in dB units). Power ratios were calculated separately for each electrode before averaging across electrodes. The stimulus-induced coherence is the difference in coherence during visual stimulation and during maintained activity.

Time periods for analysis (Table 1) were chosen for each stimulus set to minimize the effects of stimulus onset latency, stimulus offset latency, non-causal effects of the multi-taper analysis and bleed-through of residual evoked LFP. These were chosen by inspecting time-frequency power spectra at each electrode, the spectra averaged across all electrodes within individual animals, and by estimating the likely effects of residual evoked LFP, which was characterized by large increases in power across all frequencies following stimulus onset.

Table 1 here.

Control analyses for spike-LFP coherence

Sudden changes in the spiking activity and the LFP signal may result in spurious coherence because the non-stationary assumption required for multi-taper analyses is violated. To remove any contribution of this form of error, we computed spike-LFP coherence after having shuffled the trials of the LFP signal, and we report shuffled-corrected estimates of spike-LFP coherence. In addition, our estimates concentrate on coherence between spikes and the induced LFP. In additional analyses not shown, we estimated coherence between spikes and the raw LFP (which includes both evoked and induced LFP components). These yielded similar estimates of spike-LFP coherence except in the 100-200 ms following stimulus onset, where there was transient coherence across all frequencies. Finally, LFP power is increased during presentation of a visual stimulus, changing the signal-to-noise and in turn potentially distorting estimates of spike-LFP coherence. To assess the contribution of changes in LFP power to our analyses, we z-scored the LFP within each trial and analysed the spike-triggered average LFP in different frequency bands (not shown). The spike-triggered average LFP was consistent with spike-LFP coherence at frequencies below 100 Hz but not above 100 Hz, so our analyses focus on spike-LFP coherence below 100 Hz.

Current Source Density

To align laminar probe recordings we performed current source density (CSD) analysis (Nicholson and Freeman, 1975) on the evoked LFP response to long presentations of dot fields. We duplicated the uppermost and lowermost LFP recordings from each probe, converting 8 measurements into 10. We then smoothed each signal to reduce high spatial-frequency noise (Stoelzel et al., 2009):

$$LFP_s(r,p) = \frac{1}{4}\left(LFP_e(r+h,p) + 2\times LFP_e(r,p) + LFP_e(r-h,p)\right) \quad \text{Equation 3}$$

where r=depth, p=probe, h=0.2 mm (distance between contact points on a single probe); this leaves 8 measurements for each probe. CSD analyses without smoothing gave similar results. The CSD is the second spatial derivative:

$$CSD(r,p) = \frac{1}{h^2}\left(LFP_s(r+h,p) - 2\times LFP_s(r,p) + LFP_s(r-h,p)\right) \quad \text{Equation 4}$$

This process leaves 6 of the 8 recordings from each probe. For each penetration the CSDs obtained at a given recording depth were averaged across all (8) of the laterally displaced probes. For visualization purposes, the signal was smoothed with a 3x3 triangular filter. We defined the sink layer at each recording site as that which showed the strongest negative deflection in the CSD following stimulus onset; the latency to this sink was the time of the first zero-crossing following stimulus onset. We defined the 'middle layers' as all contact points aligned with the sink layer, and at points directly above (-0.2 mm) and directly below (+0.2 mm) that layer; the 'deep layers' were all contact points lying 0.4-0.8 mm below the sink layer.

Inclusion criteria

We inspected the spectrograms of LFP and induced LFP at each channel. We excluded LFP and multi-unit measurements from channels where the LFP power was not modulated by presentation of a visual stimulus, either because the channel was faulty (9/3579), or the LFP spectra during visual stimulus was indistinguishable to that for maintained activity (188/3579). Including the latter channels in the analyses did not qualitatively change the results. We also excluded one abnormal recording session using laminar probes in area MT, where 50% of the induced power in all channels was concentrated between 120-180 Hz. Tables 2 and 3 show the number of

recording sites, or pairs of sites, included in each analysis.

Table 2 and 3 here.

RESULTS

We recorded LFP signal and spiking activity from multi-electrode arrays implanted into area MT of anaesthetised marmoset monkeys. Presentation of any visual stimulus produces two changes in the LFP signal: some components ("evoked") are time locked to the stimulus onset and can be characterised by averaging the LFP across trials. Other components ("induced") are modulated by the stimulus but not time-locked to its onset. Because gamma rhythms that arise from neural circuits are more likely to be time-locked to intrinsic neural mechanisms (Whittington et al., 2011, Buzsaki and Wang, 2012), our analyses focus on the induced components of the LFP.

Stimulus-dependence of LFP response

To characterise the stimulus dependence of gamma rhythms we first measured responses to moving dot fields and moving gratings using 10x10 planar arrays. Multi-unit activity was direction selective for both gratings and dot fields, as expected, and responses at an example site are shown in Figure 1,A&B. The preferred direction of multi-unit activity at each electrode was usually the same for both stimuli (p=0.95, *Watson-Williams test*), though direction-tuning curves were generally sharper for gratings than dot fields (cf. (McDonald et al., 2014, Solomon et al., 2011).

While gratings and dot fields produced similar changes in spiking activity, they induce markedly different changes in LFP power. During presentation of dot fields, LFP power was increased across a broad band of gamma frequencies (30-250 Hz). During presentation of gratings, the LFP power increase was instead concentrated to a narrower band of frequencies, producing a 'bump' in the spectrum

between 30 and 100 Hz. This narrowband response is characteristic of oscillatory brain activity ('gamma rhythms'). The stimulus-dependence of LFP changes is apparent at individual sites (Figures 1, C&D), and it is clearest when we plot the proportional change in power during presentation of visual stimuli (Figures 1, E&F). Similar changes in the LFP power were observed in all electrodes in this animal (Figures 1, G&H), and in other animals (Figures 1, I&J).

Figure 1 here.

To provide a quantitative measure of 'broadband' and 'narrowband' LFP response, we computed the average LFP power increase over low (30-100 Hz) or high (100-250 Hz) gamma frequencies. The difference between these two measures characterises the prominence of the narrowband gamma bump. Figure 2A shows average of this metric across all electrodes in each of 5 animals, and confirms that gratings were associated with more prominent narrowband gamma. By contrast, the sum of these two measures indicates the overall strength of the broadband response, and shows that broadband gamma responses were more prominent during presentation of dot fields (Figure 2B). The larger broadband response induced by dot fields may be related to spiking activity (Ray and Maunsell, 2011a), as average firing rates were higher for dot fields (mean 137 imp/s, s.d. 67) than gratings (mean 97, s.d. 45). There was no dependence of narrowband gamma or broadband gamma response on grating spatial frequency within the range tested.

In additional analyses not shown we measured the induced LFP power at each of 12 motion directions separated by 30 degrees, using non-overlapping frequency bands (0-100 Hz in 10 Hz intervals, 100-200 Hz in 20 Hz intervals). These analyses

showed that the preferred motion direction for frequencies above 30 Hz closely matched that of the multi-unit activity recorded at the same electrode, for both gratings and dot fields. Power at frequencies below 30 Hz was on average suppressed during presentation of either dot fields or gratings, and this suppression was not tuned to motion direction.

Figure 2 here.

Depth-dependence of LFP response

The stimulus-dependent LFP response we observed was based on measurements from planar electrode arrays implanted to a depth of approximately 1 mm. The relative contribution of feedforward and local circuits to LFP response is, however, likely to depend on cortical depth, because feedforward axons target layers 3-4 in area MT(Palmer and Rosa, 2006, Spatz, 1977).

To determine the lamina structure of LFP response we implanted into area MT an array of 8 laminar probes (0.2 mm separation), each of which had 8 contact points (0.2 mm separation) at different depths. Spiking activity isolated at different sites on the same probe showed similar preferred motion direction (Figure 3A). By contrast, the preferred direction of sites on neighbouring probes (but at the same depth) showed no relationship. These results are consistent with both presence of a columnar architecture for direction tuning in area MT of marmoset, and that the array was inserted approximately perpendicular to the cortical surface.

To align cortical depth across different penetrations of the array we used current source density (CSD) analysis of response to moving dot fields (see Methods). In each penetration the CSD analysis revealed a prominent current sink that was

restricted to recording sites near the middle of each laminar probe, and was at reproducible depths across all probes. Figure 3B shows one example of the CSD analyses from each of the 3 animals in which these measurements were made; Figure 3C shows the average CSD across all penetrations in all animals, after aligning their depth to that which we observed the strongest sink. These are post-hoc analyses: CSD analyses typically use response to a brief flash of diffuse light, which we did not make. We do not know the anatomical basis of the sink: it is aligned with the channels on which multi-unit response was strongest (as is generally the case in CSD analyses: (Chen et al., 2007) (Schroeder et al., 1998), emerged 55-123 ms (mean 83, SD 21) after stimulus onset, and persisted for an average of 573 ms (SD 98).

Figure 3 here.

We used the aligned recordings to assess whether the spectra of induced LFP power depended on cortical depth (Figure 4). LFP response to dot fields showed a depth dependence: measurements from the middle contact points showed broadband gamma response while measurements from deep contact points showed more narrowband gamma response (Figures 4A&5A). LFP response to gratings, however, showed a narrowband gamma response across all depths (Figures 4C&5B). Figures 5C-F use the "narrowband" and "broadband" metrics described previously to provide a quantitative comparison of LFP across cortical depths. For gratings, these metrics showed a subtle difference across depth: both narrowband and broadband gamma were slightly greater in the middle layers compared to the deep layers (Figures 5D&F; $p=0.053$ and $p=0.063$, Student t-test). For dot fields, however, broadband gamma was much stronger in the middle layers than in the deep layers (Figure 5E, $p=0.009$), while

narrowband gamma was similar across layers (Figure 5C, p=0.66). The depth dependence of evoked spiking activity showed similar dependence on recording depth as broadband LFP response. Here we included those sites where evoked multi-unit activity was significantly different to spontaneous activity ($p<0.05$, Wilcoxon rank-sum test), and calculated average evoked spike rate across sites at the same depth. Spiking activity evoked by dot fields was stronger in the middle layers than deeper layers, while spiking activity evoked by gratings was similar across all layers (Figure 4B&D).

The measurements of LFP power reported in Figure 1, which were obtained using planar arrays, are similar to those observed near the central (sink) contact points of these laminar probes, suggesting that the planar arrays were recording near the middle layers of area MT. This is consistent with nominal depth of the planar implants and histological analyses (Solomon et al., 2015), which showed electrodes predominantly extending into layers 4-5.

Figures 4&5 here.

Spatial structure of LFP-LFP coherence

The weak gamma rhythm we observed in deeper layers of area MT during presentation of dot fields may reflect emergent gamma rhythms that are supported by local circuitry in area MT. To investigate these potential circuits further, we analysed the coherence between LFP signals recorded at pairs of contact points at the same depth (but on different probes). A coherence of 1 implies that the two LFP signals have constant phase difference (at a particular frequency) across trials; a coherence of 0 implies that the phase difference is random across trials. The amplitude of the

resting coherence, which was measured during presentation of a grey screen, decreased with distance parallel to the cortical surface (Figure 6A). The amplitude of the resting coherence did not depend on the cortical depth of the contact points used to measure it (not shown).

We found that coherence during visual stimulation depended on the depth of the contact points used to measure it. Figures 6, B&C show coherence between probes separated by 0.4 mm, during presentation of dot fields and gratings. Gamma coherence increased in all layers during presentation of gratings (p=0.62, ANOVA). During presentation of dot fields, however, gamma coherence increased only in the deep layers (p<0.05) [induced coherence at 100 Hz in the middle layers is likely due to entrainment to monitor refresh rate]. Figures 6, C&E show similar measurements but for probes separated by 1 mm. Again, gamma coherence increased primarily in deep layers, particularly during presentation of dot fields. Statistical analyses showed depth dependence of gamma coherence for dot fields (p<0.001), and weaker dependence on depth for gratings (p<0.05).

Figure 6 here.

To characterize coherence over larger spatial scales we analysed responses from the 10x10 planar arrays. The pattern of coherence across these arrays (Figure 7) was similar to the pattern of coherence across the middle contact points of the laminar probes. Gamma coherence increased during presentation of gratings but was generally suppressed when the stimulus was a dot field. The vertical striping in Figure 7A is due to strong 'ripples' in the frequency-coherence plots measured during grey screen presentations in one animal, which is likely due to the choice of multi-taper

parameters (see Methods). The increased coherence for gratings extended over very large distances, up to approximately 3.2 mm. Coherence at low frequencies (<20 Hz) induced by dot fields varied across animals: coherence increased in three animals but decreased in the other two. The narrow white line in Figure 7A arises because there were slight differences in the pattern of coherence across animals, and does not reflect a consistent increase in coherence over a narrow range of low frequencies.

Our results show that the gamma rhythms induced by gratings are present in all layers and widespread across area MT, as has been previously reported for area V1. Gamma rhythms induced by dot fields are instead weaker and the circuits that support them appear confined to the deeper layers of area MT.

Figure 7 here.

Stimulus-independence of spike-LFP coherence

Gamma rhythms have been proposed as a mechanism for modulating synaptic efficacy over short time scales (Fries, 2005, Fries, 2015), such that inputs are more effective when they arrive at a particular phase, and output spikes are therefore entrained to the gamma rhythm. If narrowband gamma rhythms always accompany entrainment, then we should see entrainment only during presentation of gratings. If, however, entrainment can be supported by either broadband or narrowband increases in gamma power, then it should be stimulus-independent. Entrainment can be captured by the spike-LFP coherence, which has a value of 1 when spikes always occur at the same phase, and a value of 0 when spikes are distributed across all phases. Contrary to our expectations, dot fields and gratings induced similar spike-LFP coherence, increasing spike-LFP coherence over a narrow band of gamma

frequencies (30-100 Hz). An example of spike-LFP coherence at a single electrode is shown in Figures 8, A&B (same electrode as Figures 1, A-F). Note that the apparent decrease in spike-LFP coherence at frequencies above 100 Hz is likely to be an artefact of stronger signal-to-noise during stimulus-evoked responses, as described in Methods, 'Control analyses for spike-LFP coherence'. Average spike-LFP coherence across all electrodes and animals was similar to these representative sites (Figures 7, C&D). The average number of spikes used for these analyses were 223 ± 95 (mean ± s.d., per electrode per trial) for evoked activity, and 18 ±13 for spontaneous activity during presentation of dot fields, respectively 152 ±73 and 32 ±16 during presentation of gratings. The phase of the spike-LFP coherence showed small but significant differences between stimulus types ($p<0.001$, Watson-Williams test; (Berens, 2009). For gamma frequencies, the average phase lead of spikes relative to the trough of the rhythm was 68.2 ± 0.3 degrees (mean ± 0.95 CI; dot fields), 67.9 ± 0.3 degrees (gratings) and 67.5± 0.3 degrees (grey screen).

Figure 8 here.

Measurement of spike-LFP coherence using spiking activity at one electrode and LFP at another showed spiking activity entrained to distant gamma rhythms (~2 mm) during presentation of gratings but not for dot fields (not shown). The patterns of coherence were consistent with the distribution of the LFP-LFP coherence shown in Figure 7. In summary, presentation of either dot fields or gratings entrains spikes to the local induced LFP at gamma frequencies, even in the absence of narrow band gamma responses. Spiking activity is entrained to gamma rhythms at distal electrodes only if the LFP at that electrode is coherent with the LFP near the recorded spikes.

Dependence of induced LFP power on image structure

The analyses above show that the LFP response in area MT depends on stimulus type (dot fields or gratings), and that this stimulus-dependence is most prominent near putative feedforward input layers. The stimulus-dependence of LFP response may therefore reflect the stimulus sensitivity of inputs from earlier visual cortical areas. Neurons in these areas are likely to be more sensitive to the local contours of gratings, and less sensitive to global motion of random dot patterns. However, gratings also have concentrated contrast energy in a small range of spatial and temporal frequencies, while dot fields have contrast energy distributed across a wide range of spatial and temporal frequencies. We therefore sought to establish whether the different LFP responses for dot fields and gratings reflect differences in orientation content or contrast.

To establish the sensitivity of LFP response to contour orientation we made measurements during presentation of synthetic textures (insets of Figure 9A), and to gratings. Presentation of static gratings of low contrast (0.125; matching the RMS contrast of the synthetic textures; Figures 9A&B) led to greater increase in narrowband gamma power than broadband gamma power, but the increase in narrow band power was less than that observed for high contrast moving gratings. The LFP power induced by a moving texture with broad orientation bandwidth (Figures 9A&D) was instead enhanced across a broad band of frequencies, and resembled the power spectrum induced by dot fields. LFP power induced by moving texture with intermediate orientation bandwidth showed an intermediate pattern (Figures 9A&C). Thus, increasing the range of orientations in a stimulus shifts the LFP power spectrum from narrowband to broadband, and increases power, producing LFP spectra that

resemble those induced by dot fields. The increase in broadband gamma power appeared consistent with pattern of spiking response to the different images: static gratings evoked lower spiking activity (mean 81 imp/s, s.d. 30), narrowband textures evoked intermediate spiking activity (mean 90, s.d. 30) and broadband textures evoked higher spiking activity (mean 112, s.d. 53).

Altering the contrast of dot fields or gratings did not affect the general pattern of the LFP responses: dot fields always induced broadband LFP responses (Figure 9E, the banding here reflects small distortions introduced by the multi-taper analysis during brief presentations, duration 0.3), while gratings always induced narrowband LFP responses (Figure 9F). The peak gamma frequency induced by gratings shifts towards lower values at low contrast, as has been observed in area V1 of macaque (Ray and Maunsell, 2010, Jia et al., 2013b).

Figure 9 here.

Potential contribution of V1 signals to the induced LFP in area MT

The visually-induced gamma rhythms in the LFP of area MT, particularly near the putative targets of feedforward input from early visual cortex, share similar properties to neural responses in those early areas. To establish if neural activity in marmoset area V1 may support these gamma rhythms, we measured LFP responses in V1 for the same stimuli. Presentation of gratings indeed induced narrowband LFP responses in area V1 that are highly similar to those observed in area MT (Figures 10A&B).

Propagation of gamma rhythms from area V1 to area MT requires rhythmic gamma to also be present in spiking discharge. To test if this is the case, we

constructed auto-correlograms (ACGs) of multi-unit and single-unit activity in area V1, obtained during the same recordings, using standard methods (Figures 10C-F). Presentation of gratings was associated with rhythmic spiking activity with a period of 0.02 s, consistent with the LFP power spectrum, in both multi-unit and single-unit activity. Multi-unit and single-unit response to dot fields did not show rhythmic behaviour at these frequencies.

Figure 10 here.

DISCUSSION

To determine the spatial structure and stimulus specificity of gamma rhythms in area MT we recorded from multi-electrode arrays implanted into anaesthetised marmoset monkeys. We found that the structure of the gamma-band LFP in area MT depends on visual stimulus and cortical layer. When the stimulus contains oriented contours, narrowband gamma rhythms were found throughout all layers; when the stimulus contains a broad range of orientations, narrowband gamma rhythms were weaker and appear limited to deeper layers.

Contribution of feedforward and local processing to gamma rhythms

Gamma rhythms are generally thought to reflect the rhythmic activity of recurrent excitatory-inhibitory networks within the area that the LFP signal is recorded from (Buzsaki and Wang, 2012, Whittington et al., 2011). Indeed, inhibition within area MT is thought important in establishing functional properties that include motion integration, motion opponency, and speed tuning (Simoncelli and Heeger, 1998, Rust et al., 2006, Tsui et al., 2010, Perrone, 2004, Perrone and Krauzlis, 2008, Qian et al., 1994, Qian and Andersen, 1994, Priebe et al., 2003, Priebe et al., 2006). Anatomical studies of area MT also show appropriate local circuitry (Anderson et al., 1998, Malach et al., 1997, Weller et al., 1984, Ahmed et al., 2012, Van Essen et al., 1981) and presence of putative inhibitory interneurons (Bourne et al., 2007, Dhar et al., 2001).

Despite the likely importance of local inhibition to functional properties of neurons in area MT, and presence of appropriate circuitry, we found limited evidence for emergence of gamma rhythms in LFP response of area MT. Gamma rhythms were

found in all layers, but they required a stimulus with oriented contours, and were prominent even for static gratings. Moving dot fields instead induced a broadband increase in LFP power, except in the deeper layers. The overall stimulus-selectivity of gamma rhythms parallels that found in recent ECoG measurements from human visual cortex, where gamma rhythms in areas V1, V2 and V3 required images with oriented contours (gratings and plaids), while noise images induced broadband increase in LFP power (Hermes et al., 2015).

We propose that the stimulus-dependent gamma rhythms near the input layers primarily reflect rhythmic activity that is inherent in the feedforward inputs to area MT. Such inputs predominantly target layers 3 and 4 of area MT (Spatz, 1977, Palmer and Rosa, 2006). Indeed, the contrast response of the gamma rhythms in these layers is similar to those observed in macaque area V1 (Ray and Maunsell, 2011a, Jia et al., 2013b), and the rhythms are similar to those already present in the output of area V1. Local neural networks may amplify the rhythmic activity of feedforward signals: about 20% of the synapses that V1 neurons make in area MT are onto putative inhibitory neurons (Anderson et al., 1998).

Gamma rhythms in the deeper layers of area MT show distinct properties from those in the layers above them, suggesting different neuronal sources. First, during presentation of gratings, gamma rhythms were coherent over longer distances in deeper layers than in upper layers. Second, presentation of dot fields induced weak gamma rhythms in the deep layers that also persisted over long distances (at least 1.0 mm). These widespread gamma rhythms in the deeper layers might be supported by long-distance horizontal connections (which are known to be present in macaque; (Ahmed et al., 2012), and may also reflect action of feedback projections, which primarily target the deeper layers of MT (Palmer and Rosa, 2006, Maunsell and van

Essen, 1983).

Stimulus-independence of spike-LFP coherence

We found that presentation of both dot fields and gratings increases entrainment of spikes to gamma rhythms in the LFP, even though dot fields induced a broadband increase in LFP power. This may suggest presence of a narrowband gamma rhythm that is masked by the broadband increase in LFP power. Entrainment of spikes to nearby LFP gamma rhythms suggests that synaptic activity (induced by a visual stimulus) is more effective at driving spiking activity when occurring at a particular phase of the gamma rhythm, as co-varying synaptic activity is the major contributor to the LFP (Buzsaki et al., 2012). The neural circuitry that gives rise to this entrainment is recruited during presentation of both gratings and dot fields, and may thus be useful in the analysis of visual motion, independent of spatial features.

We have previously shown the distribution of correlations in spiking activity across area MT of marmoset, using recordings from 10x10 planar arrays (SS Solomon et al., 2015). Analysis of shuffle-corrected cross-correlograms in that study showed strong stimulus-dependence of correlations over short time scales: sharp-peaks in the cross-correlograms persisted over long distances (at least 2.4 mm) during presentation of gratings, but not dot fields. The analyses of LFP coherence presented here show strong gamma coherence over similarly long distances during presentation of grating, and are a likely source of the long-distance spiking correlations.

LFP response and spiking activity

Similar to previous work (Ray and Maunsell, 2011a), we found that the

broadband gamma response was stronger for stimuli and recording locations associated with higher spiking activity. One explanation for this is that the broadband gamma response reflects increased excitation, which results in increased spiking activity. Alternatively, broadband gamma response may reflect the low-frequency components of the spikes themselves. We think the latter explanation unlikely, as although high frequency LFP power increased during visual stimulation, the spike-field coherence at those frequencies did not [i.e. the broadband gamma response was not temporally-locked to spiking activity] (detailed analysis shown in (Solomon, 2015)".

We show that dot fields induce an increase in broadband LFP power in the upper layers of area MT, while simultaneously reducing coherence between the LFP recorded at different electrodes, across a wide range of frequencies. This may imply that dot fields recruit localised neural circuits that are smaller than the inter-electrode distance (here 0.2-0.4 mm). The decreased LFP-LFP coherence predicts that spiking correlations will be lower during presentations of dot fields than during presentation of a grey screen. Indeed, we have previously shown that presentation of dot fields substantially reduces spike count correlations between pairs of neurons in area MT across a range of timescales (Solomon et al., 2015). During presentation of gratings, we observed increase in LFP-LFP coherence in narrowband gamma, but little change at other frequencies. Similarly, we have shown that during presentation of gratings, short time-scale spiking correlations extend over large distances across area MT.

Comparison with previous work in macaque

Our results show that LFP response in areas V1 and MT are similar in New World marmoset monkey and Old World macaque monkey. In area V1 of macaque,

strong gamma rhythms in the LFP are observed during presentation of gratings (Jia et al., 2013a, Henrie and Shapley, 2005, Frien and Eckhorn, 2000, Bartolo et al., 2011, Lima et al., 2010, Ray and Maunsell, 2011b, Ray and Maunsell, 2011a, Xing et al., 2012, Gieselmann and Thiele, 2008). During presentation of large drifting gratings, the gamma rhythms are coherent over large regions of macaque area V1 and are also coherent with spiking activity (Jia et al., 2013a, Jia et al., 2013b, Gieselmann and Thiele, 2008, Ray and Maunsell, 2011a). In area MT of macaque, LFP power at low frequencies (<30 Hz) is suppressed during visual stimulation regardless of motion direction. At higher frequencies (>30 Hz), LFP response increases with contrast and is tuned for motion direction, with tuning similar to the spiking activity of nearby neurons (Liu and Newsome, 2006, Khayat et al., 2010, Tsui and Pack, 2011). These are all consistent with our observations in area V1 and area MT of marmoset.

Our findings may help reconcile previous analyses of LFP in area MT of macaque, which have either reported increase in power across a broadband of frequencies (30-200 Hz, (Liu and Newsome, 2006, Khayat et al., 2010, Esghaei and Daliri, 2014), a weak concentration in a high gamma range (80-100 Hz; (Khawaja et al., 2009), or strong concentration of power in the gamma range (65-80 Hz; (Ray et al., 2013). Our results suggest that choice of visual stimulus is likely to account for much of the variance between these studies: indeed, those that found broadband LFP response investigated responses to dot fields, while those that found more narrowband response investigated responses to gratings.

The narrowband gamma rhythm we observed in area V1 and area MT occupies a range of frequencies (30-100 Hz) that is similar to that reported for macaque area V1 but lower than that reported for (awake) macaque area MT (Khawaja et al., 2009, Ray et al., 2013). This discrepancy may reflect species

differences, but it may also reflect anaesthesia effects, or differences in analyses. First, most anaesthetics shift EEG activity toward lower frequencies and this may skew the gamma rhythm in our experiments to lower frequencies (Silva and Antunes, 2012). Second, previous work in area MT of macaque included both evoked (stimulus-locked) and induced LFP components. The evoked LFP includes a transient response at stimulus onset that has increased power across a broadband of high frequencies; when superimposed on the induced LFP this may make the peak of the LFP response appear at higher frequencies. Consistent with this explanation, when both evoked and induced components are included in analyses, the peak frequency of the LFP response decreases with time after stimulus onset, in area MT and also in area V1 (Ray and Maunsell, 2011a, Ray et al., 2013).

Functional implications

The generation of gamma rhythms likely requires GABAergic interneurons (Cardin et al., 2009, Sohal et al., 2009) and there is hope that gamma rhythms may serve as a non-invasive measure of GABAergic function in humans. Our observations show that gamma rhythms as measured in higher cortical areas may reflect propagation of rhythms from lower areas as well as recurrent synaptic activity. This may help explain the lack of consistent relationship between the concentration of GABA and strength of gamma rhythms (Hall et al., 2010, Muthukumaraswamy et al., 2013, Saxena et al., 2013, Cousijn et al., 2014). We have further shown that appropriate stimulus manipulations can bias the LFP structure away from putative feedforward activity, which may help future work identify functional correlates of local inhibitory circuitry. Similarly, gating of feedforward rhythms may contribute to the increased gamma activity (in LFP and spiking) that is observed under attention, a

phenomenon that is clearly observed in extrastriate cortex (Fries et al., 2001, Womelsdorf et al., 2006, Gregoriou et al., 2009); in V1 attention can have variable effects on gamma activity (Chalk et al., 2010).

The entrainment of spikes to gamma frequencies may aid visual processing by amplifying signals (for example, by aiding subsequent coincidence detection) or facilitating temporal coding (Gray, 1999, Singer and Gray, 1995, Fries, 2009). We show that gamma rhythms in upper layers of MT are coherent during presentations of gratings but not dot fields. The upper layers are the major source of projections to higher levels of motion processing (Boussaoud et al., 1990): if gamma coherence is useful for encoding motion, then perceptual capacity should be impaired for broadband stimuli such as dot fields. The deeper layers are instead the major source of outputs to subcortical structures (Rockland et al., 1999, Distler and Hoffmann, 2001); the coherent gamma rhythms in deep layers may be useful in coordinating eye movements. We speculate that these laminar differences may contribute to dissociations of perceptual and motor performance. For example, it is harder to perceptually discriminate the speed of broadband than narrowband stimuli, but eye movements are faster and more reliable for broadband stimuli (Simoncini et al., 2012).

FUNDING

This work was supported by National Health & Medical Research Council of Australia (NHMRC) Grant 1005427, and by the ARC Centre of Excellence in Vision Science.

ACKNOWLEDGEMENTS

We thank S.C. Chen, N. Zeater, S.K. Cheong, and A. Pietersen for help in collecting the data, and P.R. Martin for comments on previous versions of this manuscript.

REFERENCES

AHMED, B., CORDERY, P. M., MCLELLAND, D., BAIR, W. & KRUG, K. 2012. Long-range clustered connections within extrastriate visual area V5/MT of the rhesus macaque. Cereb Cortex, 22**,** 60-73.

ANDERSON, J. C., BINZEGGER, T., MARTIN, K. A. & ROCKLAND, K. S. 1998. The connection from cortical area V1 to V5: a light and electron microscopic study. J Neurosci, 18**,** 10525-40.

BAIR, W., ZOHARY, E. & NEWSOME, W. T. 2001. Correlated firing in macaque visual area MT: time scales and relationship to behavior. J Neurosci, 21**,** 1676-97.

BARTOLO, M. J., GIESELMANN, M. A., VUKSANOVIC, V., HUNTER, D., SUN, L., CHEN, X., DELICATO, L. S. & THIELE, A. 2011. Stimulus-induced dissociation of neuronal firing rates and local field potential gamma power and its relationship to the resonance blood oxygen level-dependent signal in macaque primary visual cortex. Eur J Neurosci, 34**,** 1857-70.

BASTOS, A. M., BRIGGS, F., ALITTO, H. J., MANGUN, G. R. & USREY, W. M. 2014. Simultaneous recordings from the primary visual cortex and lateral geniculate nucleus reveal rhythmic interactions and a cortical source for gamma-band oscillations. J Neurosci, 34**,** 7639-44.

BASTOS, A. M., VEZOLI, J., BOSMAN, C. A., SCHOFFELEN, J. M., OOSTENVELD, R., DOWDALL, J. R., DE WEERD, P., KENNEDY, H. & FRIES, P. 2015. Visual areas exert feedforward and feedback influences through distinct frequency channels. Neuron, 85**,** 390-401.

BERENS, P. 2009. CircStat: a MATLAB toolbox for circular statistics. J Stat Softw, 31**,** 1-21.

BERENS, P., KELIRIS, G. A., ECKER, A. S., LOGOTHETIS, N. K. & TOLIAS, A. S. 2008. Feature selectivity of the gamma-band of the local field potential in primate primary visual cortex. Front Neurosci, 2**,** 199-207.

BOKIL, H., ANDREWS, P., KULKARNI, J. E., MEHTA, S. & MITRA, P. P. 2010. Chronux: a platform for analyzing neural signals. J Neurosci Methods, 192**,** 146-51.

BOURNE, J. A., WARNER, C. E., UPTON, D. J. & ROSA, M. G. 2007. Chemoarchitecture of the middle temporal visual area in the marmoset monkey (Callithrix jacchus): laminar distribution of calcium-binding proteins (calbindin, parvalbumin) and nonphosphorylated neurofilament. J Comp Neurol, 500**,** 832-49.

BOUSSAOUD, D., UNGERLEIDER, L. G. & DESIMONE, R. 1990. Pathways for motion analysis: cortical connections of the medial superior temporal and

fundus of the superior temporal visual areas in the macaque. J Comp Neurol, 296**,** 462-95.

BUFFALO, E. A., FRIES, P., LANDMAN, R., BUSCHMAN, T. J. & DESIMONE, R. 2011. Laminar differences in gamma and alpha coherence in the ventral stream. Proc Natl Acad Sci U S A, 108**,** 11262-7.

BUZSAKI, G., ANASTASSIOU, C. A. & KOCH, C. 2012. The origin of extracellular fields and currents--EEG, ECoG, LFP and spikes. Nat Rev Neurosci, 13**,** 407-20.

BUZSAKI, G. & WANG, X. J. 2012. Mechanisms of gamma oscillations. Annu Rev Neurosci, 35**,** 203-25.

CARDIN, J. A., CARLEN, M., MELETIS, K., KNOBLICH, U., ZHANG, F., DEISSEROTH, K., TSAI, L. H. & MOORE, C. I. 2009. Driving fast-spiking cells induces gamma rhythm and controls sensory responses. Nature, 459**,** 663-7.

CHALK, M., HERRERO, J. L., GIESELMANN, M. A., DELICATO, L. S., GOTTHARDT, S. & THIELE, A. 2010. Attention reduces stimulus-driven gamma frequency oscillations and spike field coherence in V1. Neuron, 66**,** 114-25.

CHEN, C. M., LAKATOS, P., SHAH, A. S., MEHTA, A. D., GIVRE, S. J., JAVITT, D. C. & SCHROEDER, C. E. 2007. Functional anatomy and interaction of fast and slow visual pathways in macaque monkeys. Cereb Cortex, 17**,** 1561-9.

COUSIJN, H., HAEGENS, S., WALLIS, G., NEAR, J., STOKES, M. G., HARRISON, P. J. & NOBRE, A. C. 2014. Resting GABA and glutamate concentrations do not predict visual gamma frequency or amplitude. Proc Natl Acad Sci U S A, 111**,** 9301-6.

DHAR, P., MEHRA, R. D., SIDHARTHAN, V. & SHARMA, K. 2001. Parvalbumin and calbindin D-28K immunoreactive neurons in area MT of rhesus monkey. Exp Brain Res, 137**,** 141-9.

DISTLER, C. & HOFFMANN, K. P. 2001. Cortical input to the nucleus of the optic tract and dorsal terminal nucleus (NOT-DTN) in macaques: a retrograde tracing study. Cereb Cortex, 11**,** 572-80.

ESGHAEI, M. & DALIRI, M. R. 2014. Decoding of visual attention from LFP signals of macaque MT. PLoS One, 9**,** e100381.

FRIEN, A. & ECKHORN, R. 2000. Functional coupling shows stronger stimulus dependency for fast oscillations than for low-frequency components in striate cortex of awake monkey. Eur J Neurosci, 12**,** 1466-78.

FRIES, P. 2005. A mechanism for cognitive dynamics: neuronal communication through neuronal coherence. Trends Cogn Sci, 9**,** 474-80.

FRIES, P. 2009. Neuronal gamma-band synchronization as a fundamental process in cortical computation. Annu Rev Neurosci, 32**,** 209-24.

FRIES, P. 2015. Rhythms for Cognition: Communication through Coherence. Neuron, 88**,** 220-35.

FRIES, P., REYNOLDS, J. H., RORIE, A. E. & DESIMONE, R. 2001. Modulation of oscillatory neuronal synchronization by selective visual attention. Science, 291**,** 1560-3.

FRIES, P., WOMELSDORF, T., OOSTENVELD, R. & DESIMONE, R. 2008. The effects of visual stimulation and selective visual attention on rhythmic neuronal synchronization in macaque area V4. J Neurosci, 28**,** 4823-35.

GAIL, A., BRINKSMEYER, H. J. & ECKHORN, R. 2000. Contour decouples gamma activity across texture representation in monkey striate cortex. Cereb Cortex, 10**,** 840-50.

GHARAEI, S., TAILBY, C., SOLOMON, S. S. & SOLOMON, S. G. 2013. Texture-dependent motion signals in primate middle temporal area. J Physiol, 591**,** 5671-90.

GIESELMANN, M. A. & THIELE, A. 2008. Comparison of spatial integration and surround suppression characteristics in spiking activity and the local field potential in macaque V1. Eur J Neurosci, 28**,** 447-59.

GODDARD, E., CLIFFORD, C. W. & SOLOMON, S. G. 2008. Centre-surround effects on perceived orientation in complex images. Vision Res, 48**,** 1374-82.

GRAY, C. M. 1999. The temporal correlation hypothesis of visual feature integration: still alive and well. Neuron, 24**,** 31-47, 111-25.

GREGORIOU, G. G., GOTTS, S. J., ZHOU, H. & DESIMONE, R. 2009. Long-range neural coupling through synchronization with attention. Prog Brain Res, 176**,** 35-45.

HALL, S. D., BARNES, G. R., FURLONG, P. L., SERI, S. & HILLEBRAND, A. 2010. Neuronal network pharmacodynamics of GABAergic modulation in the human cortex determined using pharmaco-magnetoencephalography. Hum Brain Mapp, 31**,** 581-94.

HENRIE, J. A. & SHAPLEY, R. 2005. LFP power spectra in V1 cortex: the graded effect of stimulus contrast. J Neurophysiol, 94**,** 479-90.

HERMES, D., MILLER, K. J., WANDELL, B. A. & WINAWER, J. 2015. Stimulus Dependence of Gamma Oscillations in Human Visual Cortex. Cereb Cortex, 25**,** 2951-9.

JIA, X., SMITH, M. A. & KOHN, A. 2011. Stimulus selectivity and spatial coherence of gamma components of the local field potential. J Neurosci, 31**,** 9390-403.

JIA, X., TANABE, S. & KOHN, A. 2013a. Gamma and the coordination of spiking activity in early visual cortex. Neuron, 77**,** 762-74.

JIA, X., XING, D. & KOHN, A. 2013b. No consistent relationship between gamma power and peak frequency in macaque primary visual cortex. J Neurosci, 33**,** 17-25.

KHAWAJA, F. A., TSUI, J. M. & PACK, C. C. 2009. Pattern motion selectivity of spiking outputs and local field potentials in macaque visual cortex. J Neurosci, 29**,** 13702-9.

KHAYAT, P. S., NIEBERGALL, R. & MARTINEZ-TRUJILLO, J. C. 2010. Frequency-dependent attentional modulation of local field potential signals in macaque area MT. J Neurosci, 30**,** 7037-48.

LIMA, B., SINGER, W., CHEN, N. H. & NEUENSCHWANDER, S. 2010. Synchronization dynamics in response to plaid stimuli in monkey V1. Cereb Cortex, 20**,** 1556-73.

LIU, J. & NEWSOME, W. T. 2006. Local field potential in cortical area MT: stimulus tuning and behavioral correlations. J Neurosci, 26**,** 7779-90.

LUI, L. L., BOURNE, J. A. & ROSA, M. G. 2007. Spatial and temporal frequency selectivity of neurons in the middle temporal visual area of new world monkeys (Callithrix jacchus). Eur J Neurosci, 25**,** 1780-92.

MAIER, A., ADAMS, G. K., AURA, C. & LEOPOLD, D. A. 2010. Distinct superficial and deep laminar domains of activity in the visual cortex during rest and stimulation. Front Syst Neurosci, 4.

MALACH, R., SCHIRMAN, T. D., HAREL, M., TOOTELL, R. B. & MALONEK, D. 1997. Organization of intrinsic connections in owl monkey area MT. Cereb Cortex, 7**,** 386-93.

MAUNSELL, J. H. & VAN ESSEN, D. C. 1983. The connections of the middle temporal visual area (MT) and their relationship to a cortical hierarchy in the macaque monkey. J Neurosci, 3**,** 2563-86.

MCDONALD, J. S., CLIFFORD, C. W., SOLOMON, S. S., CHEN, S. C. & SOLOMON, S. G. 2014. Integration and segregation of multiple motion signals by neurons in area MT of primate. J Neurophysiol, 111**,** 369-78.

MUTHUKUMARASWAMY, S. D., MYERS, J. F., WILSON, S. J., NUTT, D. J., HAMANDI, K., LINGFORD-HUGHES, A. & SINGH, K. D. 2013. Elevating endogenous GABA levels with GAT-1 blockade modulates evoked but not induced responses in human visual cortex. Neuropsychopharmacology, 38**,** 1105-12.

NICHOLSON, C. & FREEMAN, J. A. 1975. Theory of current source-density analysis and determination of conductivity tensor for anuran cerebellum. J Neurophysiol, 38**,** 356-68.

PALMER, S. M. & ROSA, M. G. 2006. Quantitative analysis of the corticocortical projections to the middle temporal area in the marmoset monkey: evolutionary and functional implications. Cereb Cortex, 16**,** 1361-75.

PERKEL, D. H., GERSTEIN, G. L. & MOORE, G. P. 1967. Neuronal spike trains and stochastic point processes. II. Simultaneous spike trains. Biophys J, 7**,** 419-40.

PERRONE, J. A. 2004. A visual motion sensor based on the properties of V1 and MT neurons. Vision Res, 44**,** 1733-55.

PERRONE, J. A. & KRAUZLIS, R. J. 2008. Spatial integration by MT pattern neurons: a closer look at pattern-to-component effects and the role of speed tuning. J Vis, 8**,** 1 1-14.

PRIEBE, N. J., CASSANELLO, C. R. & LISBERGER, S. G. 2003. The neural representation of speed in macaque area MT/V5. J Neurosci, 23**,** 5650-61.

PRIEBE, N. J., LISBERGER, S. G. & MOVSHON, J. A. 2006. Tuning for spatiotemporal frequency and speed in directionally selective neurons of macaque striate cortex. J Neurosci, 26**,** 2941-50.

QIAN, N. & ANDERSEN, R. A. 1994. Transparent motion perception as detection of unbalanced motion signals. II. Physiology. J Neurosci, 14**,** 7367-80.

QIAN, N., ANDERSEN, R. A. & ADELSON, E. H. 1994. Transparent motion perception as detection of unbalanced motion signals. III. Modeling. J Neurosci, 14**,** 7381-92.

RAY, S. & MAUNSELL, J. H. 2010. Differences in gamma frequencies across visual cortex restrict their possible use in computation. Neuron, 67**,** 885-96.

RAY, S. & MAUNSELL, J. H. 2011a. Different origins of gamma rhythm and high-gamma activity in macaque visual cortex. PLoS Biol, 9**,** e1000610.

RAY, S. & MAUNSELL, J. H. 2011b. Network rhythms influence the relationship between spike-triggered local field potential and functional connectivity. J Neurosci, 31**,** 12674-82.

RAY, S., NI, A. M. & MAUNSELL, J. H. 2013. Strength of gamma rhythm depends on normalization. PLoS Biol, 11**,** e1001477.

ROCKLAND, K. S., ANDRESEN, J., COWIE, R. J. & ROBINSON, D. L. 1999. Single axon analysis of pulvinocortical connections to several visual areas in the macaque. J Comp Neurol, 406**,** 221-50.

ROSA, M. G. & ELSTON, G. N. 1998. Visuotopic organisation and neuronal response selectivity for direction of motion in visual areas of the caudal temporal lobe of the marmoset monkey (Callithrix jacchus): middle temporal area, middle temporal crescent, and surrounding cortex. J Comp Neurol, 393**,** 505-27.

RUST, N. C., MANTE, V., SIMONCELLI, E. P. & MOVSHON, J. A. 2006. How MT cells analyze the motion of visual patterns. Nat Neurosci, 9**,** 1421-31.

SAXENA, N., MUTHUKUMARASWAMY, S. D., DIUKOVA, A., SINGH, K., HALL, J. & WISE, R. 2013. Enhanced stimulus-induced gamma activity in humans during propofol-induced sedation. PLoS One, 8**,** e57685.

SCHROEDER, C. E., MEHTA, A. D. & GIVRE, S. J. 1998. A spatiotemporal profile of visual system activation revealed by current source density analysis in the awake macaque. Cereb Cortex, 8**,** 575-92.

SILVA, A. & ANTUNES, L. 2012. Electroencephalogram-based anaesthetic depth monitoring in laboratory animals. Lab Anim, 46**,** 85-94.

SIMONCELLI, E. P. & HEEGER, D. J. 1998. A model of neuronal responses in visual area MT. Vision Res, 38**,** 743-61.

SIMONCINI, C., PERRINET, L. U., MONTAGNINI, A., MAMASSIAN, P. & MASSON, G. S. 2012. More is not always better: adaptive gain control explains dissociation between perception and action. Nat Neurosci, 15**,** 1596-603.

SINGER, W. & GRAY, C. M. 1995. Visual feature integration and the temporal correlation hypothesis. Annu Rev Neurosci, 18**,** 555-86.

SOHAL, V. S., ZHANG, F., YIZHAR, O. & DEISSEROTH, K. 2009. Parvalbumin neurons and gamma rhythms enhance cortical circuit performance. Nature, 459**,** 698-702.

SOLOMON, S. S. 2015. Population Signals in the Middle Temporal (MT) Area of Marmoset Visual Cortex. PhD Thesis, University of Sydney. http://hdl.handle.net/2123/12685

SOLOMON, S. S., CHEN, S. C., MORLEY, J. W. & SOLOMON, S. G. 2015. Local and Global Correlations between Neurons in the Middle Temporal Area of Primate Visual Cortex. Cereb Cortex, 25**,** 3182-96.

SOLOMON, S. S., TAILBY, C., GHARAEI, S., CAMP, A. J., BOURNE, J. A. & SOLOMON, S. G. 2011. Visual motion integration by neurons in the middle temporal area of a New World monkey, the marmoset. J Physiol, 589**,** 5741-58.

SPATZ, W. B. 1977. Topographically organized reciprocal connections between areas 17 and MT (visual area of superior temporal sulcus) in the marmoset Callithrix jacchus. Exp Brain Res, 27**,** 559-72.

STOELZEL, C. R., BERESHPOLOVA, Y. & SWADLOW, H. A. 2009. Stability of thalamocortical synaptic transmission across awake brain states. J Neurosci, 29**,** 6851-9.

THOMSON, D. J. 1982. Spectrum estimation and harmonic analysis. Proceedings of the IEEE, 70**,** 1055-1096.

TSUI, J. M., HUNTER, J. N., BORN, R. T. & PACK, C. C. 2010. The role of V1 surround suppression in MT motion integration. J Neurophysiol, 103**,** 3123-38.

TSUI, J. M. & PACK, C. C. 2011. Contrast sensitivity of MT receptive field centers and surrounds. J Neurophysiol, 106**,** 1888-900.

VAN ESSEN, D. C., MAUNSELL, J. H. & BIXBY, J. L. 1981. The middle temporal visual area in the macaque: myeloarchitecture, connections, functional properties and topographic organization. J Comp Neurol, 199**,** 293-326.

VAN KERKOERLE, T., SELF, M. W., DAGNINO, B., GARIEL-MATHIS, M. A., POORT, J., VAN DER TOGT, C. & ROELFSEMA, P. R. 2014. Alpha and gamma oscillations characterize feedback and feedforward processing in monkey visual cortex. Proc Natl Acad Sci U S A.

WELLER, R. E., WALL, J. T. & KAAS, J. H. 1984. Cortical connections of the middle temporal visual area (MT) and the superior temporal cortex in owl monkeys. J Comp Neurol, 228**,** 81-104.

WHITTINGTON, M. A., CUNNINGHAM, M. O., LEBEAU, F. E., RACCA, C. & TRAUB, R. D. 2011. Multiple origins of the cortical gamma rhythm. Dev Neurobiol, 71**,** 92-106.

WOMELSDORF, T., FRIES, P., MITRA, P. P. & DESIMONE, R. 2006. Gamma-band synchronization in visual cortex predicts speed of change detection. Nature, 439**,** 733-6.

XING, D., YEH, C. I., BURNS, S. & SHAPLEY, R. M. 2012. Laminar analysis of visually evoked activity in the primary visual cortex. Proc Natl Acad Sci U S A, 109**,** 13871-6.

TABLES

Table 1: Parameters used in the multi-taper spectral analyses of the LFP.

Stimulus set	A	B	C	D	E	F
Long presentations	4	7	0.4	0.05	0.25-2 s	1-1.5 s
Set 1	3	5	0.15	0.05	0.25-0.5 s	0.25-0.5 s
Set 2	2	3	0.1	0.05	0.15-0.3 s	0.15-0.3 s
Set 3	4	7	0.2	0.05	0.15-0.4 s	0.15-0.4 s

Key:
A: Time-bandwidth Product (s.Hz); B: number of tapers; C: time window (s); D: step-size (s); E: timeframe for average stimulus-induced LFP activity (relative to stimulus onset); F: timeframe for average maintained LFP activity (relative to onset of a grey screen)

Table 2: Total number of samples included in analyses

Stimulus set	Total Recording sites
10 x 10 array	
Dot fields (long presentations)	7 recordings, 5 animals, 505 electrodes, 18,505 pairs (LFP-LFP coherence) 37,010 pairs (Spike-LFP coherence)
Gratings (long presentations)	7 recordings, 5 animals, 508 electrodes 18,528 pairs (LFP-LFP coherence) 37,056 pairs (Spike-LFP coherence)
Dot fields (Set 2)	6 recordings, 5 animals, 459 electrodes
Gratings (Set 2)	3 animals, 268 electrodes
Set 3	3 animals, 250 electrodes
Laminar probes	
Dot fields (MT, long presentations)	12 penetrations, 3 animals, 729 contact points 2431 pairs (LFP-LFP coherence)
Gratings (Set 1)	11 penetrations, 2 animals, 663 contact points 2217 pairs (LFP-LFP coherence)
Dot fields (V1, long presentations)	3 penetrations, 1 animal, 189 contact points 69 single-units
Gratings (V1, long presentations)	3 penetrations, 1 animal, 189 contact points 68 single-units

Table 3: Number of samples from each animal included in analyses

Animal ID	**Dot fields (Long)**	**Gratings (Long)**	**Gratings (Set 1)**	**Dot fields (Set 2)**	**Gratings (Set 2)**	**Set 3**
10x10 array						
MA025 Contra eye	56 electrodes 1540 pairs (LFP-LFP coherence) 3080 pairs (Spike-LFP coherence)	59 electrodes 1711 pairs (LFP-LFP coherence) 3422 pairs (Spike-LFP coherence)		58 electrodes		
MA025 Ipsi eye	56 electrodes 1540 pairs (LFP-LFP coherence) 3080 pairs (Spike-LFP coherence)	59 electrodes 1711 pairs (LFP-LFP coherence) 3422 pairs (Spike-LFP coherence)		59 electrodes		
MA026 Contra eye	80 electrodes 3160 pairs (LFP-LFP coherence) 6320 pairs (Spike-LFP coherence)	78 electrodes 3003 pairs (LFP-LFP coherence) 6006 pairs (Spike-LFP coherence)				
MA026 Ipsi eye	76 electrodes 2850 pairs (LFP-LFP coherence) 5700 pairs (Spike-LFP coherence)	78 electrodes 3003 pairs (LFP-LFP coherence) 6006 pairs (Spike-LFP coherence)		82 electrodes	82 electrodes	75 electrodes
MA027	93 electrodes 4278 pairs (LFP-LFP coherence) 8556 pairs (Spike-LFP coherence)	88 electrodes 3828 pairs (LFP-LFP coherence) 7656 pairs (Spike-LFP coherence)		95 electrodes	96 electrodes	87 electrodes
MY145	67 electrodes 2211 pairs (LFP-LFP	69 electrodes 2346 pairs (LFP-LFP		69 electrodes		

	coherence) 4422 pairs (Spike-LFP coherence)	coherence) 4692 pairs (Spike-LFP coherence)				
MY147	77 electrodes 2926 pairs (LFP-LFP coherence) 5852 pairs (Spike-LFP coherence)	77 electrodes 2926 pairs (LFP-LFP coherence) 5852 pairs (Spike-LFP coherence)		96 electrodes	90 electrodes	88 electrodes
Laminar Probes MA022	1 penetration, 63 contact points, 217 pairs					
MA021	6 penetrations, 54 – 63 contact points per penetration, 162-217 pairs per penetration		6 penetrations, 60 – 64 contact points per penetration, 135-224 pairs per penetration			
MA020	5 penetrations, 58 – 63 contact points per penetration, 183-217 pairs per penetration		6 penetrations, 58 – 64 contact points per penetration, 183-224 pairs per penetration			
MA028 (V1)	3 penetrations, 63 contact points in each penetration, 217 pairs in each penetration	3 penetrations, 63 contact points in each penetration, 217 pairs in each penetration				

FIGURE CAPTIONS

Figure 1: Stimulus-induced multi-unit activity and LFP power.

(A) Peristimulus time histogram (PSTH) of multi-unit activity recorded from a single electrode during presentation of dot fields. Stimulus directions are as shown in the insets in C.

(B) PSTH during presentation of drifting sinuosoidal gratings, for the same electrode as in A. Stimulus directions are as shown in the insets in D.

(C) Average LFP power recorded from the same electrode as in A, during presentation of dot fields. Conventions as in A.

(D) Same as C but during presentation of gratings. Conventions as in A.

(E) Changes in induced LFP power relative to power during presentation of a grey screen, recorded from the same electrode as in A, during presentation of dot fields. Conventions as in A.

(F) Same as E but during presentation of gratings. Conventions as in A.

(G) Changes in induced LFP power relative to power during presentation of a grey screen, during presentation of dot fields (solid line) averaged across electrodes from one animal. Dotted curves represent 95% confidence intervals.

(H) Same as G but during presentations of gratings. Conventions as in G.

(I) Changes in induced LFP power relative to power during presentation of a grey screen, during presentation of dot fields (solid line) averaged across electrodes and all animals. Conventions as in G.

(J) Same as I but during presentation of gratings.

Figure 2: Comparison of the narrowband gamma and broadband gamma induced by dot fields and gratings

(A) Difference in stimulus-induced LFP power between gamma (30 – 100 Hz) and high gamma (100 – 250 Hz) frequencies. The range of gamma and high gamma frequencies is shown in the inset. Scatter plot compares the average difference across electrodes for each animal induced by gratings and dot fields.

(B) Sum of the stimulus-induced LFP power at gamma and high gamma frequencies. Scatter plot compares the average sum across electrodes for each animal induced by gratings and dot fields.

Figure 3: Current source density analysis

(A) Distribution of the difference in preferred motion direction, for multi-unit activity at pairs of recording sites on arrays of 8 laminar probes. (Top) Distribution for 767 pairs of contact points on the same laminar probe. (Bottom) Distribution for 942 pairs of contact points at the same depth, but on different probes within an array.

(B) Example current source density (CSD) analyses from each animal in which recordings were made using laminar probes. Inset shows intensity scale of the CSD measurement.

(C) Aligned CSD averaged across all 12 recordings sites in 3 animals. Measurements for each recording site are normalized to the greatest source/sink value between 0.5 s before and 0.5 s after stimulus onset. Inset shows intensity scale of the CSD.

Figure 4: Depth dependence of stimulus-induced LFP power. Measurements using an array of laminar probes.

(A) Laminar profile of induced LFP power during presentation of dot fields.

Measurements are averaged across 729 contact points (12 penetrations, 3 animals). Power is relative to that during presentation of a grey screen. Laminar distance is relative to the sink layer. Inset shows intensity scale.

(B) Multi-unit spiking activity during presentation of dot fields. Measurements show the difference in spiking activity during presentation of dot fields and presentation of grey screens. Measurements are averaged across 683 contact points (12 penetrations, 3 animals).

(C) LFP power during presentation of gratings. Conventions as in B. Measurements are averaged across 663 contact points (11 penetrations, 2 animals).

(D) Multi-unit spiking activity during presentation of gratings. Measurements show the difference in spiking activity during presentation of gratings and presentation of grey screens. Measurements are averaged across 503 contact points (11 penetrations, 2 animals).

Figure 5: Comparison of the LFP power response in middle and deep layers.

(A) Changes in induced LFP power relative to power during presentation of a grey screen, during presentation of dot fields for contact points in the middle (n=281) and deep (n=209) layers.

(B) Changes in induced LFP power relative to power during presentation of a grey screen, during presentation of gratings for contact points in the middle (n=259) and deep (n=190) layers. For presentation purposes, the spectra were smoothed with a three-point averaging filter ([1/3 1/3 1/3]) and power at low frequencies (<20 Hz) is not shown. Power at low frequencies dipped to about -1 dB and -0.5 dB for middle and deep layers.

(C) Narrowband gamma response in the middle and deep layers during presentation

of moving dot fields. Same samples as A.

(D) Narrowband gamma response during presentation of moving gratings. Same samples as B.

(E) Broadband gamma response during presentation of moving dot fields. Same samples as in A.

(J) Broadband gamma response during presentation of moving gratings. Same samples as in B.

Figure 6: Depth dependence of stimulus-induced LFP-LFP coherence. Measurements using an array of laminar probes.

(A) Average LFP-LFP coherence during presentation of a grey screen from pairs of contact points at the same depth (n=2431). Different curves represent pairs separated by different distances as shown in the legend.

(B) Laminar profile of relative LFP-LFP coherence between during presentation of dot fields (left) and gratings (right). Measurements shown here are for 523 (dot fields) and 480 (gratings) pairs of contact points separated by 0.4 mm. Coherence is relative to that during presentation of a grey screen. Intensity scale is shown in the inset.

(C) Same as B but for measurements of contact points separated by 1.0 mm (n=254 for dot fields, n=231 for gratings). Conventions as in B.

(D) Box plot showing the LFP-LFP coherence in the gamma band (30-100 Hz) averaged across recording sites as a function of depth for contact points separated by 0.4 mm during presentation of dot fields (left) and gratings (right). Boxes show the range between the first and third quartiles, grey lines show the medians, whiskers show the range between 2.7 standard deviations above and below the median and grey crosses show outliers. Same samples as in B.

(E) Same as D but for contact points separated by 1.0 mm. Same samples as in B.

Figure 7: LFP-LFP coherence between pairs of electrodes. Measurements obtained using the 10x10 array.

(A) Change in LFP-LFP coherence during presentation of moving dot fields. Coherence is relative to that during presentation of a grey screen. Measurements are averaged across 18,505 electrode pairs from 5 animals. Intensity scale is shown in the inset.

(B) Same as A, but for measurements during presentation of moving gratings. Measurements are averaged across 18,528 electrode pairs from 5 animals.

(C) Box plot showing the LFP-LFP coherence in the gamma band (30-100 Hz) averaged across animals as a function of distance during presentation of moving dot fields. Boxes show the range between the first and third quartiles, grey lines show the medians, whiskers show the range between 2.7 standard deviations above and below the median and grey crosses show outliers. Same samples as in A.

(D) Same as C but for measurements during presentation of moving gratings. Same samples as in B.

Figure 8: Stimulus-induced spike-LFP coherence at a single electrode.

(A) Example spike-LFP coherence from a single electrode on the 10x10 array, during presentation of moving dot fields. Inset shows direction of motion. Same electrode as Figures 1A-F.

(B) Same as A, but during presentation of moving gratings.

(C) Change in spike-LFP coherence during presentation of dot fields. Coherence is relative to that during presentation of grey screens. Measurements are averaged across

stimulus directions and across 505 electrodes from 5 animals.

(D) Same as C but during presentation of gratings (508 electrodes, 5 animals).

Figure 9: Dependence of LFP power on contour orientations and contrast.

(A) Stimulus-induced LFP power during presentation of moving gratings and static gratings, and moving textures with a bandwidth of orientation contours (circular SD: 25 degrees and 6 degrees); all stimuli were presented at contrast of 0.125. Power is relative to that during presentation of a grey screen. Measurements are averaged across 250 electrodes from implants of the 10x10 array in 3 animals.

(B) Stimulus-induced LFP power during presentation of static gratings as a function of time and frequency. Same samples as in A.

(C) Stimulus-induced LFP power during presentation of moving textures with low bandwidth of contour orientations (circular SD: 6 degrees) as a function of time and frequency. Same samples as in A.

(D) Stimulus-induced LFP power during presentation of moving textures with high bandwidth of contour orientations (circular SD: 25 degrees) as a function of time and frequency. Same samples as in A.

(E) Stimulus-induced LFP power during presentation of moving dot fields of varying contrast. Power is relative to that during presentation of a grey screen. Measurements are averaged across 459 electrodes from 5 animals.

(F) Stimulus-induced LFP power during presentation of moving gratings of varying contrast. Power is relative to that during presentation of a grey screen.

Figure 10: V1 responses during presentations of dot fields and gratings.

(A) Black solid curve shows stimulus-induced LFP power during presentations of

moving dot fields in area V1. Power is relative to the power during presentation of grey screens. Dotted curves represent 95% confidence intervals. Measurements are averaged across 189 contact points from one animal. Corresponding data from area MT is show in in grey.

(B) Black solid curve shows stimulus-induced LFP power during presentations of moving gratings in area V1. Power is relative to the power during presentation of grey screens. Dotted curves represent 95% confidence intervals. Measurements are averaged across 189 contact points from one animal. Corresponding data from area MT is show in in grey.

(C) Average auto-correlogram (ACG; binwidth 0.1 ms) of multi-unit activity in area V1 during presentations of dot fields. For clarity, the peak at zero lag which extends to a value of 1 has been truncated. Same samples as in A.

(D) Same as C but for measurements during presentation of moving gratings. Same samples as in B.

(E) Average ACG (binwidth 1 ms) for single-unit activity in area V1 during presentations of moving dot fields. Measurements are averaged across 69 single-units.

(D) Same as E but for measurements during presentations of moving gratings. Measurements are averaged across 68 single-units.

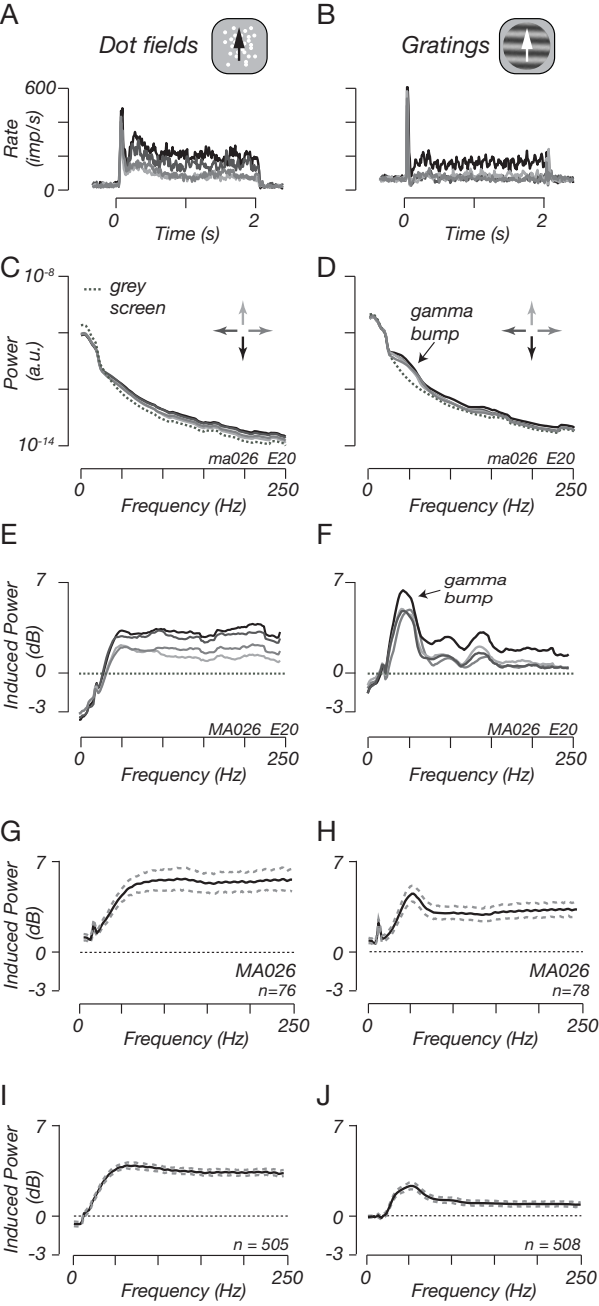
A
Dot fields
B
Gratings
600
Rate
(imp/s)
0
0
2
Time (s)
0
2
Time (s)
C
D
10^{-8}
grey
screen
Power
(a.u.)
10^{-14}
gamma
bump
ma026 E20
0
250
Frequency (Hz)
ma026 E20
0
250
Frequency (Hz)
E
F
7
Induced Power
(dB)
0
-3
gamma
bump
MA026 E20
0
250
Frequency (Hz)
MA026 E20
0
250
Frequency (Hz)
G
H
7
Induced Power
(dB)
0
-3
MA026
n=76
0
250
Frequency (Hz)
MA026
n=78
0
250
Frequency (Hz)
I
J
7
Induced Power
(dB)
0
-3
n = 505
0
250
Frequency (Hz)
n = 508
0
250
Frequency (Hz)

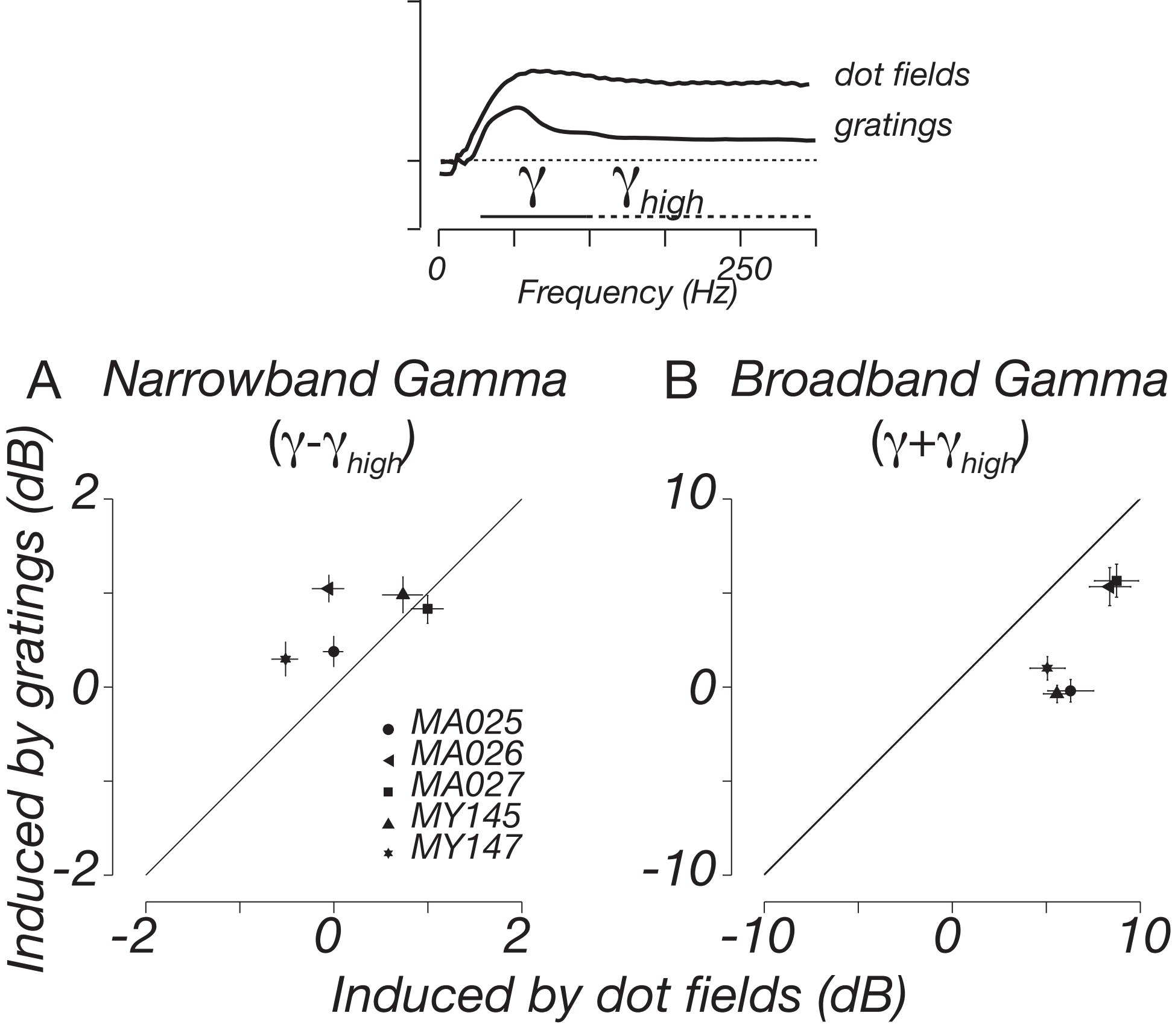
dot fields
gratings
γ
γ high
0
250
Frequency (Hz)
A Narrowband Gamma
(γ-γ high)
B Broadband Gamma
(γ+γ high)
Induced by gratings (dB)
Induced by dot fields (dB)
2
0
-2
10
0
-10
MA025
MA026
MA027
MY145
MY147

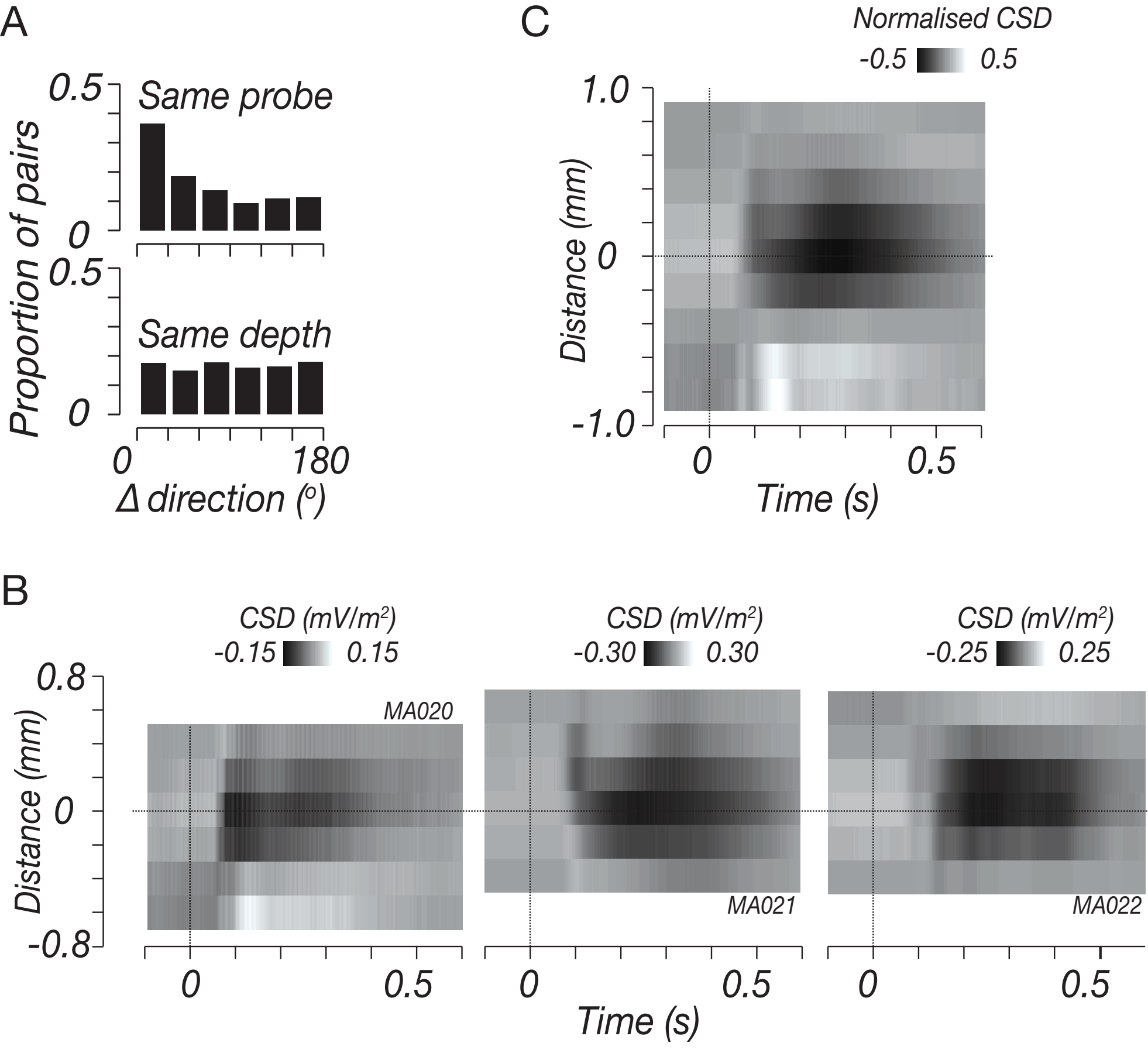
A
0.5
Same probe
0
0.5
Same depth
0
Proportion of pairs
0
180
Δ direction (°)
C
Normalised CSD
-0.5
0.5
1.0
0
-1.0
Distance (mm)
0
0.5
Time (s)
B
CSD (mV/m²)
-0.15
0.15
CSD (mV/m²)
-0.30
0.30
CSD (mV/m²)
-0.25
0.25
0.8
0
-0.8
Distance (mm)
MA020
MA021
MA022
0
0.5
0
0.5
0
0.5
Time (s)

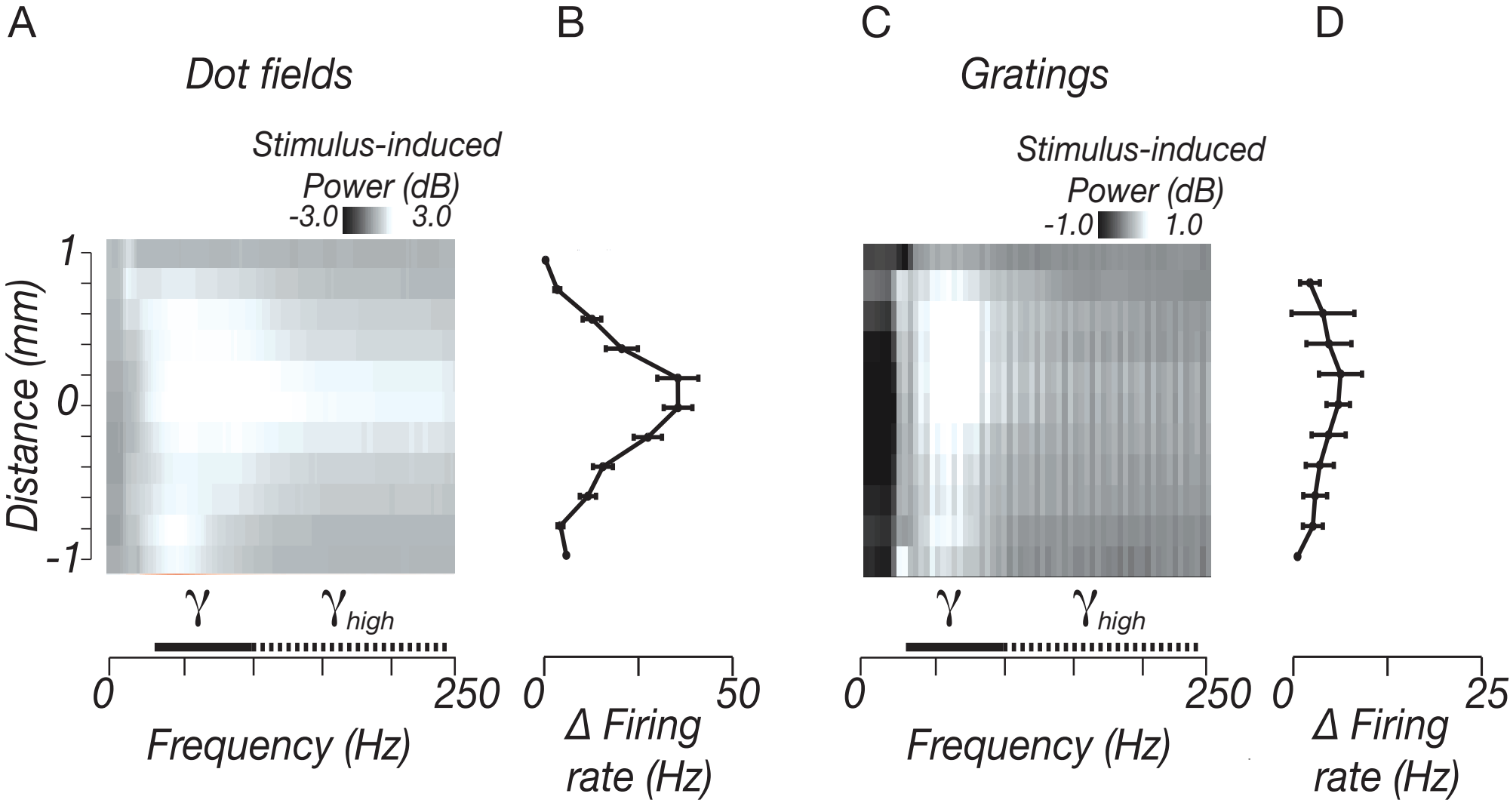
A
Dot fields
Stimulus-induced
Power (dB)
-3.0
3.0
1
0
-1
Distance (mm)
γ
γ high
0
250
Frequency (Hz)
B
0
50
Δ Firing
rate (Hz)
C
Gratings
Stimulus-induced
Power (dB)
-1.0
1.0
γ
γ high
0
250
Frequency (Hz)
D
0
25
Δ Firing
rate (Hz)

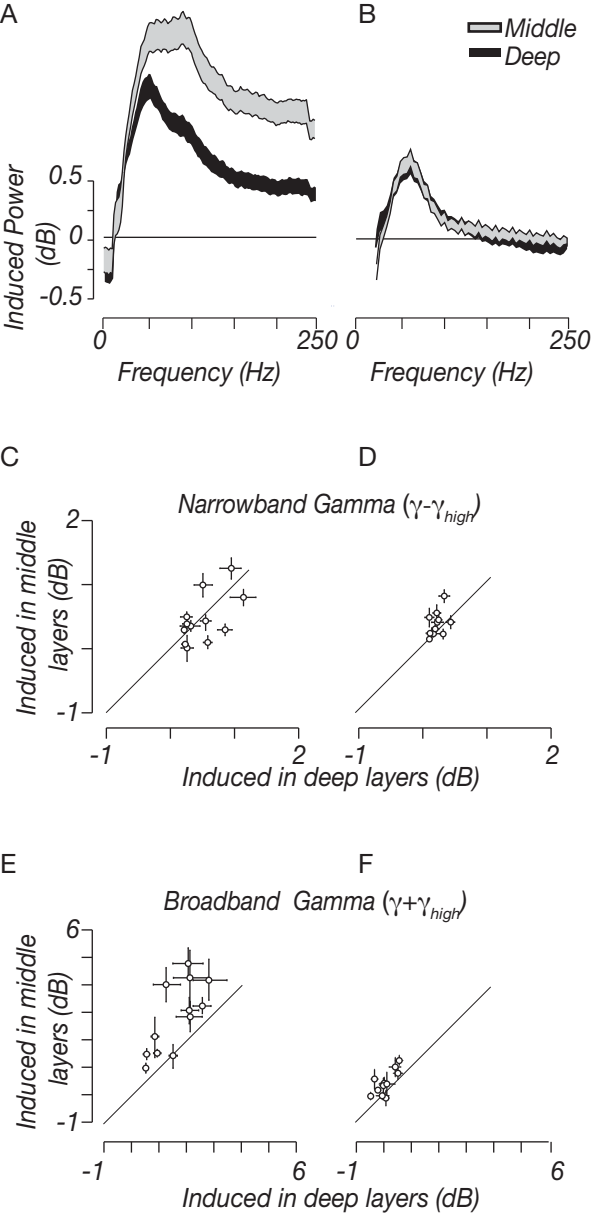
A
B
Middle
Deep
Induced Power (dB)
0.5
0
-0.5
0
250
Frequency (Hz)
0
250
Frequency (Hz)
C
D
Narrowband Gamma (γ-γhigh)
Induced in middle layers (dB)
2
-1
-1
2
Induced in deep layers (dB)
E
F
Broadband Gamma (γ+γhigh)
Induced in middle layers (dB)
6
-1
-1
6
Induced in deep layers (dB)

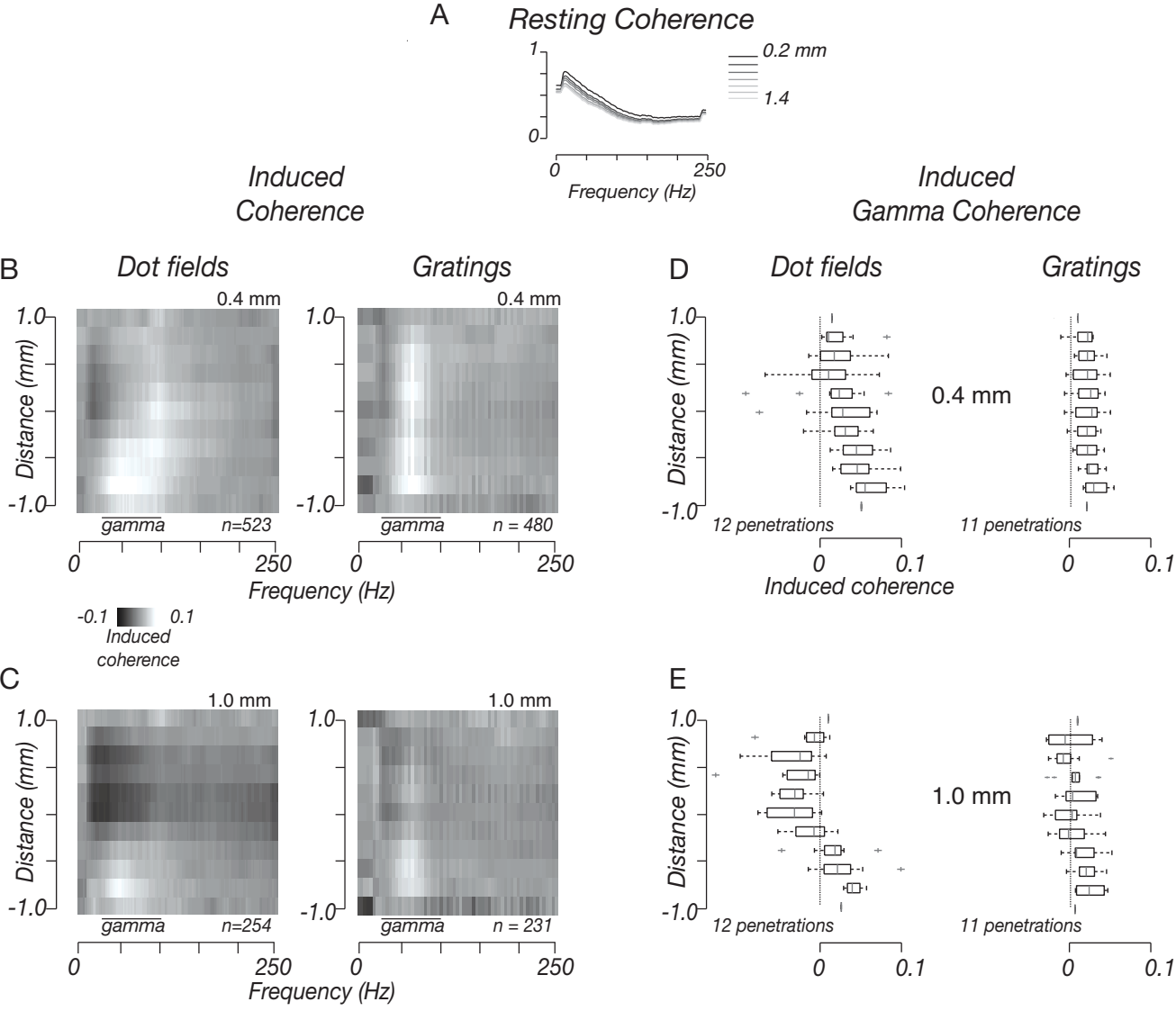
A
Resting Coherence
1
0
0.2 mm
1.4
0
250
Frequency (Hz)
Induced
Coherence
Induced
Gamma Coherence
B
Dot fields
Gratings
0.4 mm
0.4 mm
1.0
-1.0
Distance (mm)
gamma
n=523
gamma
n = 480
0
250
Frequency (Hz)
-0.1
0.1
Induced
coherence
C
1.0 mm
1.0 mm
gamma
n=254
gamma
n = 231
D
Dot fields
Gratings
0.4 mm
12 penetrations
11 penetrations
0
0.1
Induced coherence
E
1.0 mm
12 penetrations
11 penetrations

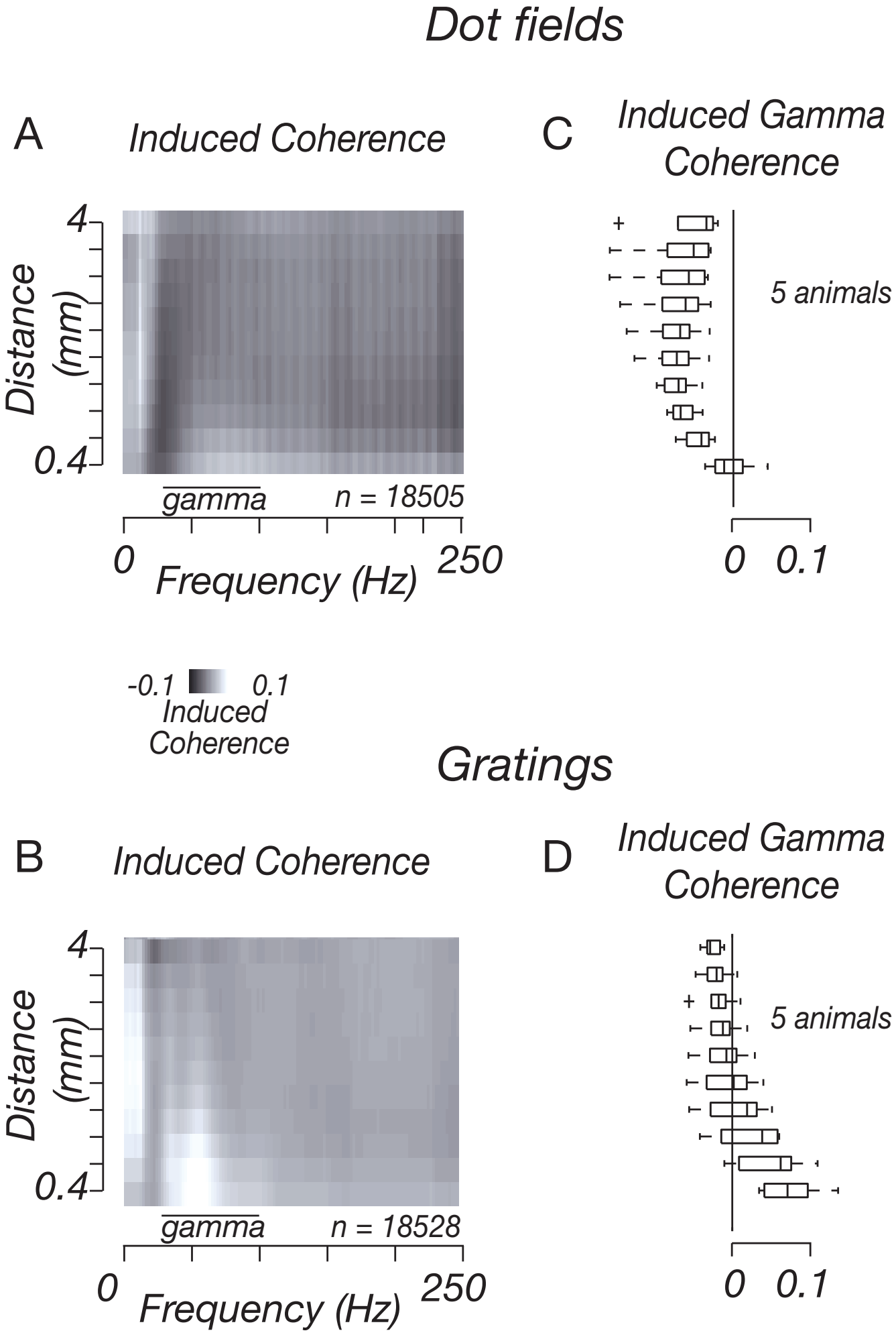
Dot fields
A
Induced Coherence
4
Distance
(mm)
0.4
gamma
n = 18505
0
Frequency (Hz)
250
C
Induced Gamma
Coherence
5 animals
0
0.1
-0.1
0.1
Induced
Coherence
Gratings
B
Induced Coherence
4
Distance
(mm)
0.4
gamma
n = 18528
0
Frequency (Hz)
250
D
Induced Gamma
Coherence
5 animals
0
0.1

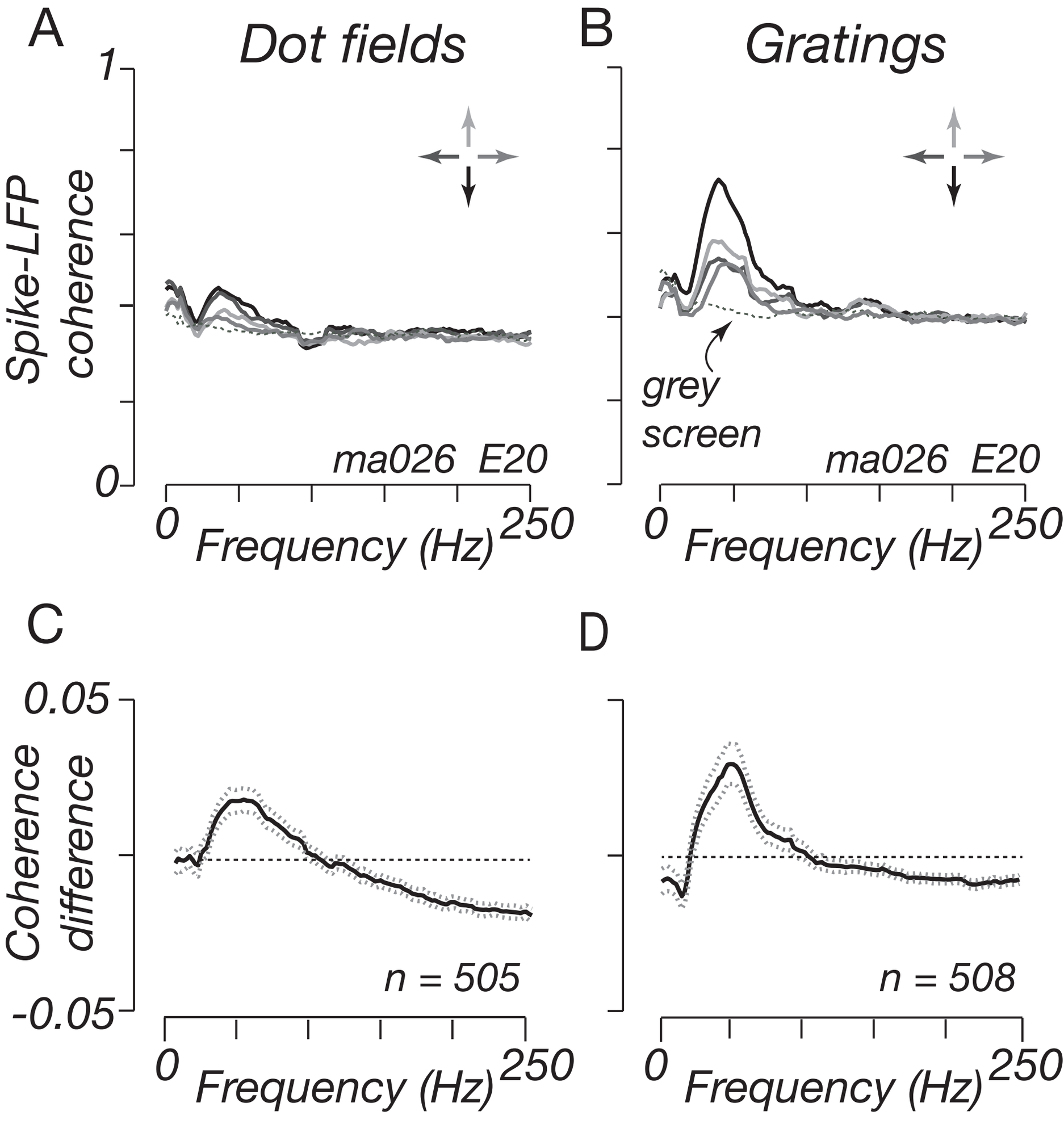
A
Dot fields
B
Gratings
1
0
Spike-LFP coherence
ma026 E20
0
Frequency (Hz)
250
grey screen
C
D
0.05
-0.05
Coherence difference
n = 505
n = 508

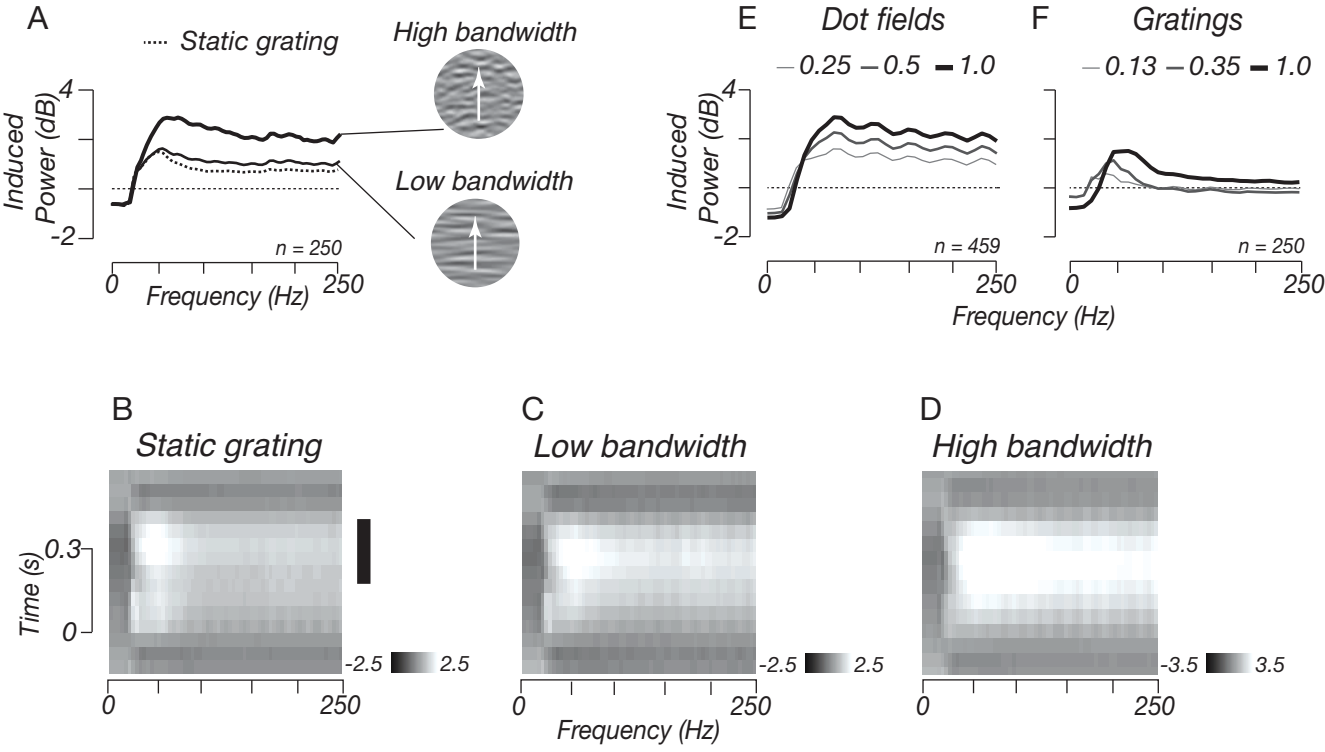
A
Static grating
High bandwidth
Low bandwidth
Induced Power (dB)
4
-2
n = 250
0
Frequency (Hz)
250
E
Dot fields
0.25
0.5
1.0
Induced Power (dB)
4
-2
n = 459
0
250
F
Gratings
0.13
0.35
1.0
n = 250
0
250
Frequency (Hz)
B
Static grating
C
Low bandwidth
D
High bandwidth
Time (s)
0.3
0
-2.5
2.5
-2.5
2.5
-3.5
3.5
0
250
0
250
0
250
Frequency (Hz)

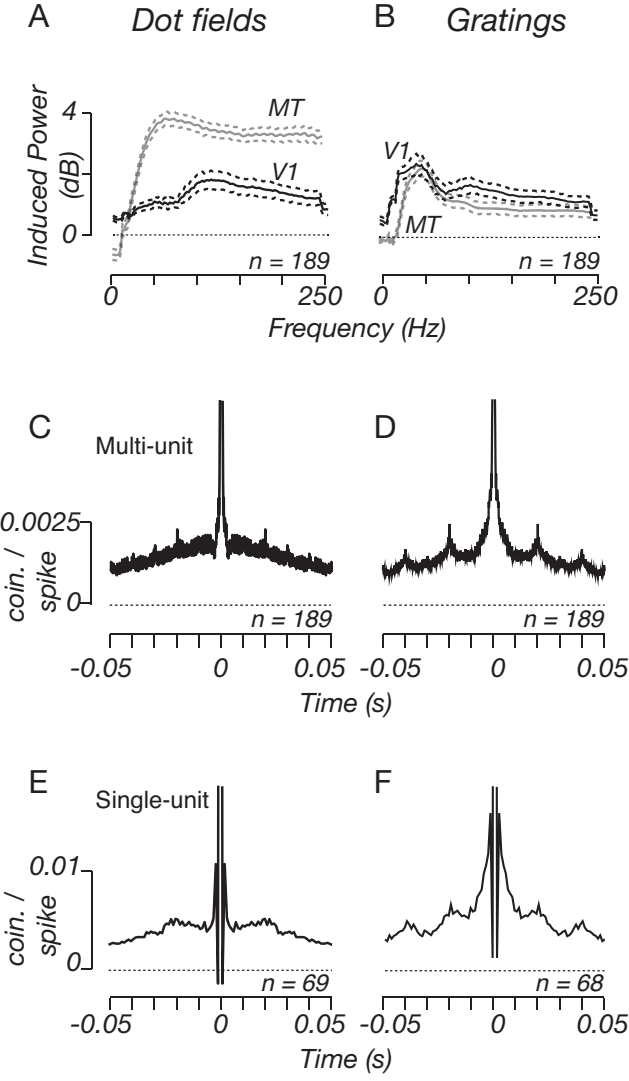
A
Dot fields
B
Gratings
Induced Power (dB)
4
0
MT
V1
n = 189
0
250
V1
MT
n = 189
0
250
Frequency (Hz)
C
Multi-unit
0.0025
coin. / spike
0
n = 189
-0.05
0
0.05
D
n = 189
-0.05
0
0.05
Time (s)
E
Single-unit
0.01
coin. / spike
0
n = 69
-0.05
0
0.05
F
n = 68
-0.05
0
0.05
Time (s)